Inorganic Chemistry

pubs.acs.org/IC Article

Experimental and Theoretical Evidence for an Unusual Almost Triply Degenerate Electronic Ground State of Ferrous Tetraphenylporphyrin

Maxime Tarrago, Christina Römelt, Joscha Nehrkorn, Alexander Schnegg, Frank Neese,* Eckhard Bill,* and Shengfa Ye*

Cite This: *Inorg. Chem.* 2021, 60, 4966–4985 Read Online

ACCESS | Metrics & More | Article Recommendations | Supporting Information

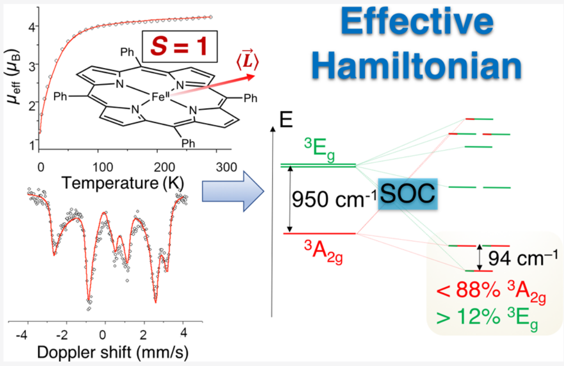

ABSTRACT: Iron porphyrins exhibit unrivalled catalytic activity for electrochemical CO_2-to-CO conversion. Despite intensive experimental and computational studies in the last 4 decades, the exact nature of the prototypical square-planar [Fe^{II}(TPP)] complex (**1**; TPP^{2-} = tetraphenylporphyrinate dianion) remained highly debated. Specifically, its intermediate-spin (S = 1) ground state was contradictorily assigned to either a nondegenerate $^3A_{2g}$ state with a $(d_{xy})^2(d_{z^2})^2(d_{xz,yz})^2$ configuration or a degenerate $^3E_g^\theta$ state with a $(d_{xy})^2(d_{xz,yz})^3(d_{z^2})^1/(d_{z^2})^2(d_{xy})^1(d_{xz,yz})^3$ configuration. To address this question, we present herein a comprehensive, spectroscopy-based theoretical and experimental electronic-structure investigation on complex **1**. Highly correlated wave-function-based computations predicted that $^3A_{2g}$ and $^3E_g^\theta$ are well-isolated from other triplet states by ca. 4000 cm^{-1}, whereas their splitting Δ_{A-E} is on par with the effective spin–orbit coupling (SOC) constant of iron(II) (≈400 cm^{-1}). Therfore, we invoked an effective Hamiltonian (EH) operating on the nine magnetic sublevels arising from SOC between the $^3A_{2g}$ and $^3E_g^\theta$ states. This approach enabled us to successfully simulate all spectroscopic data of **1** obtained by variable-temperature and variable-field magnetization, applied-field ^{57}Fe Mössbauer, and terahertz electron paramagnetic resonance measurements. Remarkably, the EH contains only three adjustable parameters, namely, the energy gap without SOC, Δ_{A-E}, an angle θ that describes the mixing of $(d_{xy})^2(d_{xz,yz})^3(d_{z^2})^1$ and $(d_{z^2})^2(d_{xy})^1(d_{xz,yz})^3$ configurations, and the $\langle r_d^{-3}\rangle$ expectation value of the iron d orbitals that is necessary to estimate the ^{57}Fe magnetic hyperfine coupling tensor. The EH simulations revealed that the triplet ground state of **1** is genuinely multiconfigurational with substantial parentages of both $^3A_{2g}$ (<88%) and ^3E_g (>12%), owing to their accidental near-triple degeneracy with Δ_{A-E} = +950 cm^{-1}. As a consequence of this peculiar electronic structure, **1** exhibits a huge effective magnetic moment (4.2 μB at 300 K), large temperature-independent paramagnetism, a large and positive axial zero-field splitting, strong easy-plane magnetization ($g_\perp \approx 3$ and $g_\parallel \approx 1.7$) and a large and positive internal field at the ^{57}Fe nucleus aligned in the xy plane. Further in-depth analyses suggested that $g_\perp \gg g_\parallel$ is a general spectroscopic signature of near-triple orbital degeneracy with more than half-filled pseudodegenerate orbital sets. Implications of the unusual electronic structure of **1** for CO_2 reduction are discussed.

1. INTRODUCTION

Transition-metal complexes supported by macrocyclic ligands, such as porphyrins, phthalocyanines, and corroles, have been utilized as (pre)catalysts for the activation of a wide range of small molecules, such as CO_2, O_2, and H_2.[1] It is thus of great interest to elucidate their electronic structures as a prerequisite to understanding structure–activity relationships and underlying chemical principles, the subject of intense research efforts worldwide.[2] In this regard, electrochemical CO_2-to-CO conversion catalyzed by complex [Fe(TPP)] (**1**; TPP^{2-} = tetraphenylporphyrinate dianion) and its derivatives displays exceedingly high efficiency and nearly exclusive product selectivity.[3] It was found that [Fe(*o*-TMA)]$^{4+}$ (*o*-TMA^{2+} = *o*-*N*,*N*,*N*-trimethylanilinium porphyrinate dication) exhibits the highest catalytic activity of all relevant catalysts reported thus far.[4]

The experimental work reported by Savéant, Robert, and co-workers demonstrated that complex **1** undergoes two successive one-electron reductions to generate [Fe(TPP)]$^-$ (**1**$^-$) and [Fe(TPP)]$^{2-}$ (**1**$^{2-}$) and that the latter species, formally a Fe(0) compound, is the actual CO_2 reductant.[3] We

Received: January 6, 2021
Published: March 19, 2021

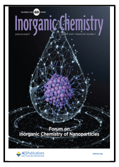

https://doi.org/10.1021/acs.inorgchem.1c00031
Inorg. Chem. 2021, 60, 4966–4985

recently studied the electronic structures of reduced species $\mathbf{1}^-$ and $\mathbf{1}^{2-}$ in great detail using ^{57}Fe Mössbauer, X-ray absorption, and resonance Raman spectroscopy coupled with quantum-chemical calculations. The results established that both reduction steps are ligand-centered. Throughout the series, the Fe center retains an intermediate-spin (S_{Fe} = 1) Fe(II) state and is antiferromagnetically coupled to the nascent porphyrin radicals generated by the reduction; i.e., complexes $\mathbf{1}^-$ and $\mathbf{1}^{2-}$ are best formulated as $[\mathrm{Fe^{II}(TPP^{\bullet 3-})}]^-$ and $[\mathrm{Fe^{II}(TPP^{\bullet\bullet 4-})}]^{2-}$ rather than $[\mathrm{Fe^{I}(TPP^{2-})}]^-$ and $[\mathrm{Fe^{0}(TPP^{2-})}]^{2-}$, respectively.[5]

In the case of parent complex **1**, although early studies[6] have assigned a quintet ground state, consensus has been finally reached that the ground state is a triplet. Specifically, the room-temperature effective magnetic moments (μ_{eff}) measured for various crystalline forms obtained by different preparation procedures range from 4.0 to 4.4 μ_{B} (Bohr magnetons).[7] The values are considerably lower than the spin-only value for S = 2 (4.9 μ_{B}) but substantially surpass that expected for S = 1 (2.8 μ_{B}). An S = 2 d^6 configuration would inevitably populate the Fe $d_{x^2-y^2}$-centered molecular orbital (MO) that is strongly σ-antibonding with respect to the interaction between the Fe center and the four porphyrin N donors. Here, the xy plane is defined as the plane of the porphyrin ligand. In fact, the Fe–$\mathrm{N_{TPP}}$ bond distance (1.97 Å) determined by X-ray crystallography for **1**[7] is significantly shorter than those found for the related high-spin (S = $^5/_2$) ferric porphyrin complex, $[\mathrm{Fe^{III}(TPP)Cl}]$ (2.06 Å)[8] and $[\mathrm{Zn^{II}(TPP)}]$ (2.03–2.04 Å).[9] For the latter two complexes, the Fe $d_{x^2-y^2}$ MO is singly and doubly occupied, respectively. The bond metrics thus provide strong experimental support for an S = 1, instead of an S = 2, ground state of complex **1**.[10] The intermediate-spin ground state is in accordance with its square-planar coordination geometry, where the Fe $d_{x^2-y^2}$ MO lies at much higher energy than the remaining essentially nonbonding d_{xy}, d_{xz}, d_{yz}, and d_{z^2} orbitals and, hence, is unpopulated. As such, four low-lying triplet electron configurations can be envisioned (Scheme 1), namely, (a) $^3A_{2g}$ with a $(d_{xy})^2(d_{z^2})^2(d_{xz,yz})^2$ configuration, (b) $^3E_g(A)$ $(d_{xy})^2(d_{z^2})^1(d_{xz,yz})^3$, (c) $^3E_g(B)$ $(d_{xy})^1(d_{z^2})^2(d_{xz,yz})^3$, and (d) $^3B_{2g}$ $(d_{xy})^1(d_{z^2})^1(d_{xz,yz})^4$ (Scheme 1). Here, the symmetry of each state is labeled by the irreducible representations of the D_{4h} point group.

Despite intense experimental studies over the course of the last 4 decades, the intermediate-spin ground state of **1** that can be assigned to either $^3A_{2g}$ or a degenerate ^3E_g state has not been completely established. Zero-field ^{57}Fe Mössbauer measurements on **1**[11] and resonance Raman studies on a related complex, $[\mathrm{Fe^{II}(OEP)}]$ ($\mathrm{OEP^{2-}}$ = octaethylporphyrinate dianion),[12] suggested the ^3E_g ground state with predominant parentage of the $^3E_g(A)$ configuration. On the contrary, experimental investigations using X-ray diffraction,[13] ^{1}H NMR,[14] applied-field ^{57}Fe Mössbauer spectroscopy,[15] and, in particular, magnetometry[7] all attributed the $^3A_{2g}$ ground state to **1**.

Theoretical studies have led to a number of contradictory assignments as well, even for calculations using highly correlated wave-function-based ab initio approaches. Early CASSCF/CASPT2 (CASSCF = complete-active-space self-consistent field; CASPT2 = complete-active-space with second-order perturbation theory) computations on $[\mathrm{Fe^{II}(Por)}]$ ($\mathrm{Por^{2-}}$ = porphyrinate dianion) erroneously predicted a quintet ground state,[16] but later, more accurate CCSD(T) [CCSD(T) = coupled cluster with single, double, and perturbative triple excitations] calculations arrived at a triplet-ground-state assignment.[17] Very impressive stochastic CASSCF calculations including all porphyrin π orbitals in the active space, recently reported by Alavi and co-workers,[18] yielded $^3E_g(A)$ about 175 cm^{-1} lower in energy than $^3A_{2g}$. Qualitatively, the same conclusion was reached by earlier computations using configuration interaction[19] and multi-reference Möller–Plesset perturbation theory.[16,20] By contrast, recent CASSCF/CASPT2 and CCSD(T) calculations published by Radón,[17] Pierloot,[21] Bistoni,[22] and their co-workers all favored the $^3A_{2g}$ ground state, with an energy gap of at most 800 cm^{-1} between the $^3E_g(A)$ and $^3A_{2g}$ states (Table S1). It should be noted that the aforementioned energy separations all fall into the uncertainty range of the computational methodologies employed.

Scheme 1. Four Low-Lying Triplet Electron Configurations of 1[a]

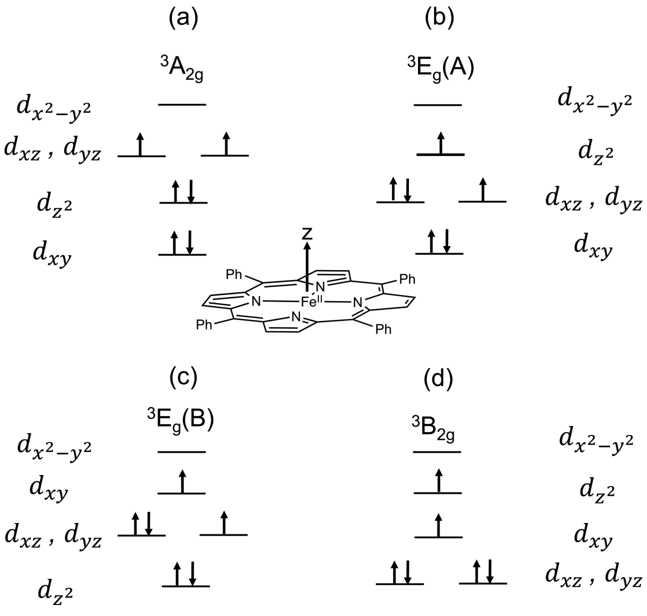

[a] Of note, inversion of the d_{z^2} and d_{xy} orbital energies leads to the same configuration in parts a and d. For both cases, only one of the two possible energy orders is displayed in the scheme.

Taken together, the earlier work is indicative of a situation in which neither experiments nor quantum-chemical calculations alone could reach an unambiguous assignment of $^3A_{2g}$ or ^3E_g to the ground state of **1**. In this work, we present a combined spectroscopy-based theoretical and experimental study on complex **1**, based on variable-temperature and variable-field (VTVH) magnetization, applied-field ^{57}Fe Mössbauer, and terahertz electron paramagnetic resonance (THz-EPR) measurements. After an unsuccessful attempt to reproduce all spectroscopic details with the usual spin Hamiltonian (SH) formalism, we designed an effective Hamiltonian (EH) operating on the nine-dimensional Hilbert space spanned by the energetically closely spaced $^3A_{2g}$ and ^3E_g states. This approach enabled us to successfully simulate all magnetization and ^{57}Fe Mössbauer experimental data and derive meaningful parameters closely related to the electronic structure. Further in-depth analyses revealed the correlation of the electronic structures and magnetic properties of **1**. In particular, our analyses demonstrated how the unusual spectroscopic parameters are a characteristic signature of a near-triple orbital degeneracy, as opposed to double orbital degeneracy. Of note, the latter case attracted much attention recently, particularly in the field of molecular magnetism. Finally, we discussed ramifications of the peculiar electronic structure of **1** on the mechanism of its catalyzed electrochemical CO_2 reduction.

2. EXPERIMENTAL PROCEDURES

2.1. Synthesis. All reactions were carried out in an inert-glovebox argon atmosphere. Stabilizer-free tetrahydrofuran (THF) was purchased at Acros Organics. Before use, it was degassed by a freeze−pump−thaw technique (three cycles), stirred over sodium for 2 days, and stored over a molecular sieve (4 Å). Heptane was purchased at Acros Organics, degassed by bubbling argon through it for 1 h, and stored over a molecular sieve (4 Å). [Fe(TPP)Cl] was purchased at Sigma-Aldrich with 95% purity (porphin residue). Sodium anthracenide was prepared by a previously described procedure.[23] After reduction, all samples were stored at −40 °C inside the glovebox. [Fe(TPP)] was prepared according to the procedure published by Scheidt and co-workers.[24]

[Fe(TPP)(THF)$_2$]. [Fe(TPP)Cl] (100 mg, 0.142 mmol, 1 equiv) was dissolved in THF (12 mL). Sodium anthracenide (0.2 M solution, 0.71 mL, 1 equiv) was added slowly via a syringe to prevent local excess of the reducing agent. The solution was stirred at room temperature for 30 min, then filtered over a poly(tetrafluoroethylene) syringe filter, layered with heptane (48 mL), and set aside for crystallization at −40 °C for 2−3 days. The mother liquor is removed, and the remaining solid is washed with a little heptane (3 × 1 mL). UV−vis (2-MeTHF, RT): λ_{max} 425, 545, and 605 nm.

[Fe(TPP)]. [Fe^{II}(TPP)(THF)$_2$] is dried at 100 °C in high vacuum (10^{-2} mbar) for 60 min. Thermogravimetric measurements confirm the loss of two THF molecules from the THF adduct: $m_{\text{before thermogravimetry}}$ = 9.3 mg; $m_{\text{after thermogravimetry}}$ = 7.56 mg; Δm_{calcd} for [M − 2THF] = 1.73 mg; Δm_{exp} = 1.74 mg. UV−vis (2-MeTHF, RT): λ_{max} 425, 545, and 605 nm.

2.2. Magnetic Susceptibility Measurements. Magnetic susceptibility data were measured from powder samples of a solid material immobilized in eicosane in the temperature range 2−300 K by using a Superconducting Quantum Interference Device (SQUID) with a field of 1 T (MPMS-7, Quantum Design; calibrated with a standard palladium reference sample; error <2%). Multiple-field variable-temperature magnetization measurements were done at 1, 4, and 7 T also in the range of 2−300 K with the magnetization equidistantly sampled on a $1/T$ temperature scale.

2.3. ^{57}Fe Mössbauer Spectroscopy. ^{57}Fe Mössbauer spectra were recorded on conventional spectrometers with alternating constant acceleration of the γ source. The minimum experimental line width was 0.24 mm/s (full width at half-height). The sample temperature was maintained constant in either an Oxford Instruments Variox cryostat or a cryogen-free, closed-cycle Mössbauer magnet cryostat from Cryogenic Ltd. The latter is a split-pair superconducting magnet system for applied fields up to 7 T. The temperature of the sample can be varied in the range 1.7−300 K. The field at the sample is perpendicular to the γ beam. The ^{57}Co/Rh source (1.8 GBq) was positioned at room temperature inside the gap of the magnet system at the zero-field position by using a reentrant bore tube. The detector was an Ar/10% CH_4-filled end-window-type proportional counter for the zero-field measurements and a Si drift diode (150 mm^2 SDD CUBE) of an AXAS-M1 system from Ketek GmbH with a vacuum-tight 200 mm stainless steel finger, which was inserted into the cryostat to position the diode also in the gap of the magnet. Isomer shifts are quoted relative to Fe metal at 300 K.

2.4. THz EPR. Frequency-domain Fourier transform (FD-FT) THz-EPR investigations were performed at the THz beamline of the synchrotron BESSY II, Helmholtz-Zentrum Berlin. This spectrometer allows for THz-EPR measurements from 0.1 to 11 THz (∼3−370 cm^{-1}), employing a fully evacuated high-resolution Fourier transform infrared spectrometer (IFS 125, Bruker), a superconducting high-field magnet (Oxford Spectromag 4000; B_0 = +11 to −11 T) with variable-temperature insert (T = 1.5−300 K) and liquid-He-cooled bolometer detectors. A detailed description of the spectrometer can be found elsewhere;[25] experimental procedures are described in the Supporting Information. SH simulations were performed with *EasySpin*[26] and its extensions for frequency-domain EPR.[27]

2.5. Computational Details. Three distinct porphyrin conformations, namely, ruffled, saddled, and planar, have been found for crystal structures of complex **1** (ruffled and saddled) and of its derivative [Fe(TTP)] (TTP^{2-} = tetratolylporphyrinate anion; planar).[7] The varying core conformations have slightly different Fe−N bond lengths and disparate packing modes, which may lead to their different electronic structures, a behavior observed for a high-spin dicyano[*meso*-tetrakis(2,4,6-triethylphenyl)porphyrinato]iron(III) complex.[28] Because the crystal structure of **1** was not resolved in our laboratory, calculations were performed on the aforementioned three porphyrin conformations.

Starting from the crystal structures[7] of each core conformation (ruffled, saddled, and planar), only the positions of the H atoms were optimized in the gas phase by using the BP86 functional in combination with the def2-TZVP basis set for all atoms.[29,30] D3BJ corrections due to Grimme were employed for dispersion corrections.[31] Calculations were sped up by using the resolution identity approximation.[32] Normal SCF (1 × 10^{-6} Eh), normal geometry convergence criteria, and grid 5 were used for these calculations.

For each of the aforementioned core conformations, CASSCF calculations[33] were performed in the gas phase in conjunction with Ahlrich's def2-TZVP basis set for all atoms. These calculations were state-averaged over the four lowest triplet and four lowest quintet states. The normal convergence criteria were selected (energy convergence threshold 1 × 10^{-7} Eh and orbital gradient convergence threshold 1 × 10^{-3}). A grid 6 was used for all calculations. The quasi-restricted orbitals[34] from a single-point density functional theory (DFT) calculation were used for the initial guess of each CASSCF calculation. For each case, the active space consisted of 8 electrons distributed into 11 orbitals. In addition to five 3d orbitals of the Fe center, the bonding counterpart of the Fe $d_{x^2-y^2}$ MO was added to the active space to account for Fe−TPP covalent interactions. Besides these six orbitals, the second d shell was included in the active space because of the well-known double-shell effect.[35] The active orbitals are shown in Figure S1. On top of the CASSCF wave functions, a dynamical correlation was recovered by using the strongly contracted second-order N-electron valence perturbation theory (NEVPT2).[36] All calculations were performed using the *ORCA*, version 4.0, package.[37]

3. RESULTS AND DISCUSSION

3.1. Experimental Characterizations. *Magnetometry Measurements.* To explore the electronic structure of **1**, we first carried out VTVH magnetometry investigations on a powder sample. As shown in Figure 1, the effective magnetic moment μ_{eff} determined at 298 K (4.24 μ_B) is markedly higher than the spin-only value for a triplet state (2.8 μ_B), in agreement with earlier studies.[7] At high temperatures, μ_{eff} does not level off up to room temperature, reflecting a strong non-Curie behavior for **1**. Instead, the high-temperature slope of μ_{eff} indicates a considerable temperature-independent paramagnetism (TIP) contribution to the magnetic susceptibility (χ).[38] Similar non-Curie behavior has been previously observed for related square-planar Fe(II) compounds using ^{1}H NMR spectroscopy.[39] Below ca. 120 K, μ_{eff} drops precipitously, typical of systems having strong axial zero-field splitting (ZFS). In accordance with this notion, isofield magnetization curves measured at varying applied fields (B_{ext} = 1, 4, and 7 T) display a strong nesting behavior (inset of Figure 1).

To simulate the SQUID data, we employed the usual SH for triplets, given by

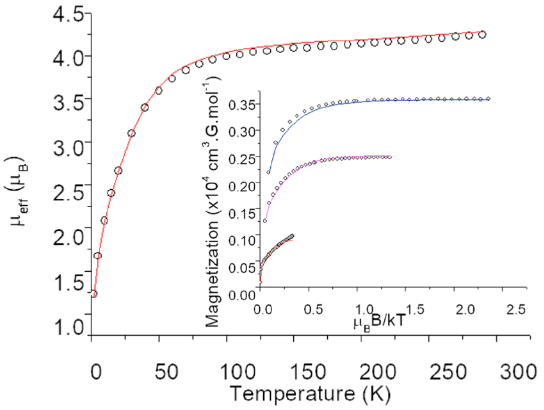

Figure 1. SH fit of the effective magnetic moment of **1** at variable temperature and under 1 T (red) and (inset) isofield magnetization curves under 1 T (red), 4 T (magenta), and 7 T (blue). The dots represent experimental measurements, and the solid lines represent the SH fits with the following parameters: $g_\perp = 3.07$, $g_\parallel = 1.70$, $D = 94$ cm^{-1}, $E/D = 0$, and $\chi_{\text{TIP}} = 1000 \times 10^{-6}$ emu. 7.9% $S = 2$ impurities were taken into account in the simulations.

$$H_{\text{el,SH}} = D\left[\hat{\tilde{S}}_z^{2} - \frac{1}{3}\tilde{S}(\tilde{S}+1) + \frac{E}{D}(\hat{\tilde{S}}_x^{2} - \hat{S}_y^{2})\right] + \mu_B\overrightarrow{B_{\text{ext}}}\cdot\mathbf{g}\cdot\vec{\tilde{S}} \qquad (1)$$

where $\tilde{S} = 1$ is the pseudospin, D and E/D are the axial and rhombicity ZFS parameters, and $\mathbf{g}$ is the Zeeman $\mathbf{g}$ matrix (more details are given in the Supporting Information). During the simulation, E/D was fixed to zero, according to the effective D_{4h} symmetry of **1**. A global simulation yielded a reasonable fit with $D = 94$ cm^{-1}, $g_\perp = 3.07$, $g_\parallel = 1.70$ ($g_{\text{av}} = 2.70$), and $\chi_{\text{TIP}} = 1000 \times 10^{-6}$ emu (Figure 1). Note that the TIP correction is not included in eq 1. The simulation indeed confirms a rather large ZFS in complex **1**, and the determined D and g_{av} are consistent with those reported before for two different crystalline forms of **1** ($D = 70$ and 108 cm^{-1}; $g_{\text{av}} = 2.94$ and 2.77).[7ab] The resulting g_{av} deviates substantially from the spin-only value, $g_e \approx 2$, which accounts for the unusually high μ_{eff} of 4.24 μ_B at 298 K because, in high-temperature limit, the spin-only effective moment would be $\mu_{\text{eff}} = g_{\text{av}}\sqrt{\tilde{S}(\tilde{S}+1)}\,\mu_B$. The large TIP correction confirms the non-Curie behavior of χ at high temperatures. In addition, we found that the sample contains 7.9% of $S = 2$ impurities, likely because of the residual presence of [Fe(TPP)(THF)$_2$] ($S = 2$).[40] Alternatively, the impurities might be high-spin Fe(III) products generated by air oxidation, as documented in earlier publications.[6,7] Simulations with the same parameters, except 5.5% $S = {}^5/_2$ impurity instead of 7.9% $S = 2$ impurity, also yielded a global fit of similar quality (Figure S2). Either way, the presence of impurities explains the deviation of the isofield magnetization curve under 1 T from a plateau-shaped response, typically expected for a system with large positive D and low E parameters.

Although the quality of the fits was satisfactory, the huge D and g_{av} values thus obtained cast doubt on the validity of the SH formalism. In principle, the SH only can be applied to systems featuring energetically well-isolated, nondegenerate electronic ground states without first-order orbital angular momenta.[41] In the present case, such a large magnitude of D, in fact, signals the existence of low-lying excited states, as elaborated by McGarvey and Telser for related ferrous complexes.[42] Furthermore, the TIP correction corresponds to an ad hoc term in the SH and is used to approximate field-induced unavoidable mixing of the ground and excited states, corresponding to quadratic Zeeman effects.[38] The TIP value found for **1** is an order of magnitude higher than those typically observed for systems with orbitally nondegenerate ground states,[43] which further corroborates the existence of low-lying excited states for **1**. As a consequence, **1** may even have an orbitally nearly degenerate ground state. Congruent with this reasoning, **1** indeed possesses sizable unquenched orbital angular momentum, as evidenced by the determined g_{av} factor significantly exceeding g_e.

THz-EPR Spectroscopy. The zero-field THz-EPR spectrum of **1** (Figure 2) exhibits a single resonance at 94.4 cm^{-1}. With increasing applied fields, this resonance splits into two components, with one being blue-shifted and the other being red-shifted. The zero-field position of this resonance provides an accurate measure of the energy splitting ΔE of the low-lying triplet and, hence, corresponds to its (absolute) value. For a triplet in zero field, two EPR transitions are allowed. The fact

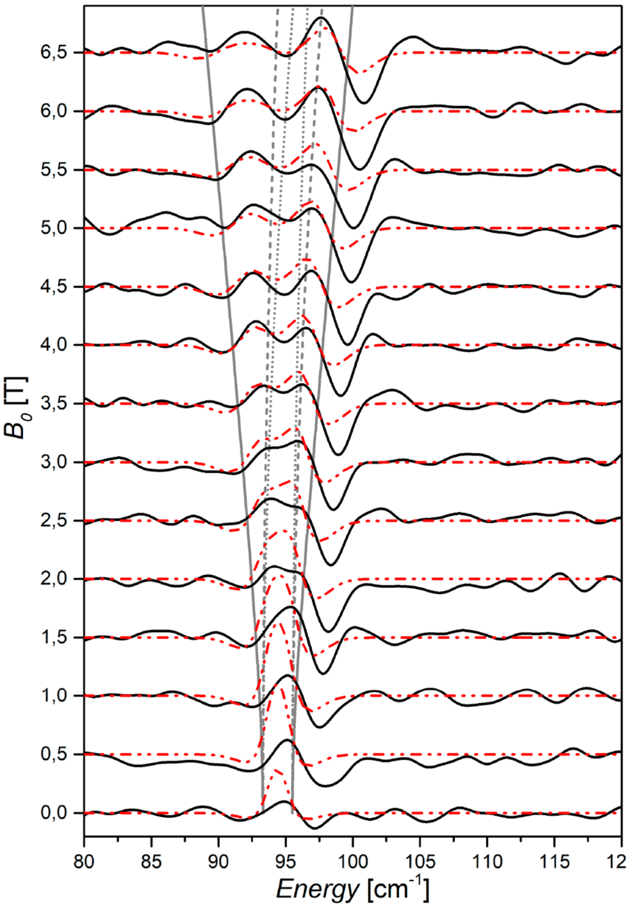

Figure 2. Experimental FD-FT THz-EPR spectra of **1** (black line). Spectra are shown as magnetic field division spectra, where the spectrum for B_0 is obtained by dividing a spectrum measured at $B_0 + 1$ T by a spectrum at B_0. Spectra are rescaled and offset according to the applied magnetic field B_0. Simulations with the SH parameters: $D = 94.4$ (± 1) cm^{-1}, $E = 1.1$ (± 1) cm^{-1}, and $g_\parallel = 1.70$ are shown as red dash-dotted lines. Gray lines indicate calculated transition energies for magnetic fields applied along the x (dashed), y (dotted), and z (solid) axes.

that we observe only one transition indicates that two of the three states are (almost) degenerate. In the language of the SH, this corresponds to a negligible E/D value. Nevertheless, simultaneous SH simulations of zero-field and field-dependent spectra allowed an estimate of E. Further, while $g_\perp$ cannot be determined accurately, because the variation of $g_\perp$ (for $g_\perp < 4$) does not discernibly affect the quality of the simulations, a good assessment of $g_\parallel$ was possible. The best agreement between the experimental spectra and SH simulations was obtained with the following parameters (Figure 2): $D = 94.4$ ($\pm$1) cm^{-1}, $E = 1.1$ ($\pm$1) cm^{-1}, and $g_\parallel = 1.70$; therefore, E/D = 0.00−0.02.

^{57}Fe Mössbauer Spectroscopy. The zero-field ^{57}Fe Mössbauer spectrum of a powder sample of complex **1** measured at 80 K (Figure S4) showed a well-resolved quadrupole doublet with an isomer shift (δ) of 0.56 mm/s and a quadrupole splitting ($|\Delta E_Q|$) of 1.31 mm/s. The δ value is consistent with those (0.52−0.57 mm/s) reported earlier for **1**,[7] as well as those for related complexes [Fe^{II}(OEP)] (0.62 mm/s) and [Fe^{II}(OEC] (0.63 mm/s; OEC^{2-} = *trans*-7,8-dihydrooctaethylporphyrinate dianion).[44] The quadrupole splitting determined for our sample is also comparable to that found for complex **1** having a ruffled core (1.51 mm/s),[7,15] as well as those for [Fe^{II}(OEP)] (1.71 mm/s[44] and 1.60 mm/s[45,46]).

To explore the magnetic hyperfine interaction of the ^{57}Fe nuclei with the electronic system of complex **1**, VTVH ^{57}Fe Mössbauer studies were conducted. As shown in Figure 3, the magnetic splitting of the spectra recorded at 1.7 K is moderately large but strongly field-dependent. Each spectrum shows a unique pattern determined by competing nuclear Zeeman and electric quadrupole interactions of unique strength. The occurrence of not more than six resolved lines is characteristic of fast paramagnetic relaxation. In this limit, the internal fields at the iron nuclei, B_{int}, arising from (field-induced) magnetic moments of the electronic system, are Boltzmann-weighted averages of the contributions from the individual magnetic sublevels of the electronic ground state. The internal fields depend on the direction of the applied field with respect to the molecular frame, and the effective splitting of the spectra is determined by the vector addition of internal and applied fields. Finally, the envelope of the spectra results from additional powder averan age.

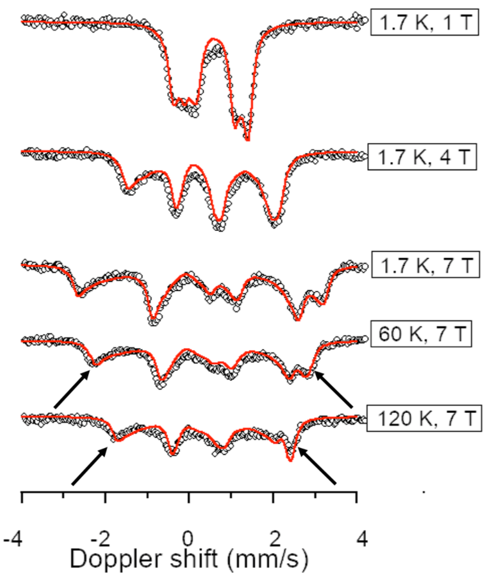

Figure 3. SH fit of ^{57}Fe Mössbauer spectra of a powder sample of **1** at 1.7 K under 1 T, at 1.7 K under 4 T, at 1.7 K under 7 T, at 60 K under 7 T, and at 120 K under 7 T. Dots represent the experimental measurements, and red solid lines represent the SH fit, with the following parameters: $D = 94$ cm^{-1}, $E/D = 0$, $g_\perp = 3.07$, $g_\parallel = 1.70$, $A_\perp/g_N\beta_N = +50.0$ T, $A_\parallel = 0$, $\Delta E_Q = +1.31$ mm/s, $\eta = V_{zz}/(V_{xx} - V_{yy}) = 0$, and $\delta = 0.56$ mm/s. Black arrows indicate slight but systematic misfits of the magnetic hyperfine splitting at elevated temperatures.

In view of the large D of the low-lying triplet of the electronic system, the magnetic Mössbauer spectra recorded at 1.7 K (Figure 3, traces 1−3 from top) only can probe the properties of the lowest magnetic level (corresponding to "M_S = 0" of pseudospin $\tilde{S} = 1$ in the SH picture). Indeed, the weak magnetic splitting of the spectrum obtained with B_{ext} = 1 T at 1.7 K renders just a magnetically perturbed quadrupole doublet (Figure 3, topmost trace) because of almost vanishing internal fields at this condition. This corresponds to a nearly vanishing induced magnetic moment of the lowest level at a weak applied field. In the SH picture, this feature, as well as the subsequent significant increase of B_{int} at 4 and 7 T at 1.7 K (traces 2 and 3 from top), would be typical of an integer spin system ($S = 1$) with a large positive D, leading to a lowest-lying "$M_S = 0$" level. Interestingly, the strong increase of the magnetic Mössbauer splitting with the applied field suggests the presence of a *positive* internal field. This is particularly unusual for Fe(II) and always originates from the dominant contribution of an unquenched orbital moment to the magnetic hyperfine coupling, as will be detailed in section 3.4.

The 7 T spectrum at 1.7 K (Figure 3, trace 3 from top) approaches the typical six-line pattern anticipated for the high-field limit of mixed magnetic and electric hyperfine interactions,[46] where the nuclear Zeeman splitting strongly dominates over the quadrupole shifts of nuclear levels because of the presence of a strong induced internal field. In this situation, the intensity of the $\Delta M_I = 0$ lines in the Mössbauer spectrum (lines 2 and 5 from left to right) is determined by the direction of the hyperfine field with respect to that of the incident γ beam. This holds true even for powder samples, as long as the paramagnetic centers show strong magnetic anisotropy. Here for **1**, the strong $\Delta M_I = 0$ lines in the 7 T/1.7 K spectrum indicate particularly easy-plane (xy) magnetization of the lowest magnetic sublevel.

The shift of the inner four Mössbauer lines of the 7 T spectrum at 1.7 and 60 K with respect to the outer two lines represents a *negative quadrupole shift*. However, in the actual high-field limit of hyperfine interactions, the quadrupole shift in first order only arises from the component of the electric-field-gradient (EFG) tensor pointing along the dominating internal field. Because the internal field is predominantly oriented in the xy plane, as inferred above, only the (negative) V_{xx} and V_{yy} components of the EFG tensor are effective in the measurement. Because the EFG is a traceless tensor, the sign of the main component V_{zz} must be positive and so is ΔE_Q. Here we can safely assume that the EFG tensor is collinear, with the principal axes of the electronic Hamiltonian describing the magnetic properties of **1** because of the effective D_{4h} symmetry.

On the basis of the qualitative understanding discussed above, we simulated all VTVH Mössbauer spectra using an $\tilde{S}$ = 1 SH. To do so, the SH shown in eq 1 was augmented with a nuclear SH ($H_{nuc,SH}$), consisting of the electric quadrupole (H_Q), the nuclear Zeeman (H_Z), and the magnetic hyperfine coupling interactions ($H_{HFC,SH}$). In addition, isomer shifts, δ, are just uniformly added to all Mössbauer transition energies (H_δ).

$$H_{\mathrm{nuc,SH}} = H_\delta + H_\mathrm{Q} + H_\mathrm{Z} + H_{\mathrm{HFC,SH}} \tag{2a}$$

$$H_\mathrm{Q} = \frac{eQ}{2I(2I-1)}(V_{zz}\hat{I}_z^{\,2} + V_{xx}\hat{I}_x^{\,2} + V_{yy}\hat{I}_y^{\,2}) \tag{2b}$$

$$H_\mathrm{Z} = -\beta_\mathrm{N} g_\mathrm{N} \overrightarrow{B_{\mathrm{ext}}}\cdot\vec{I} \tag{2c}$$

$$H_{\mathrm{HFC,SH}} = \vec{I}\cdot\mathbf{A}\cdot\vec{\tilde{S}} \tag{2d}$$

Here, e is the elementary charge of the proton, Q the quadrupole moment of the nucleus (taken as 0.16 Barns), I the nuclear spin quantum number, $\hat{I}_\alpha$ the α component of the nuclear spin angular momentum operator, g_N the nuclear g factor for ^{57}Fe (0.179 for the ground state $I = {}^1/_2$ and −0.102 for the excited state $I = {}^3/_2$), β_N the nuclear magneton, and **A** the hyperfine coupling tensor (more details are available in the Supporting Information). Because of the high symmetry of the molecule, the EFG and **A** tensors have the same principal axis system as the **g** matrix and **D** tensor. Moreover, the x and y components of these matrices were taken to be equivalent by symmetry. For the Mössbauer simulations, the electronic SH parameters were fixed to $D = 94$ cm^{-1}, $E/D = 0$, $g_\perp = 3.07$, $g_\parallel = 1.70$, and only **A** was allowed to vary (Figure 3). Note that $A_\parallel$ cannot be properly resolved as expected for systems with very large positive D values and was arbitrarily set to zero. The low-temperature (1.7 K) spectra at varying fields can be fitted satisfactorily with a large and positive value, $A_\perp/g_\mathrm{N}\beta_\mathrm{N} = +50.0$ T, which generates an internal field along the same direction as the external field $\left(\overrightarrow{B_{\mathrm{int}}} = -\mathbf{A}\langle\vec{S}\rangle/g_\mathrm{N}\beta_\mathrm{N}\right)$ and, hence, results in the drastic increase of the magnetic splitting with applied fields. However, the temperature dependence of the internal fields cannot be properly reproduced by the SH simulations, as can be seen from small but systematic misfits at elevated temperatures marked by arrows in Figure 3. Apparently, the SH formalism requires that the **A** tensors of the "$M_S = \pm 1$" and "$M_s = 0$" magnetic sublevels should be different. In fact, the same problem was encountered in an earlier study. Lang and co-workers circumvented this problem by using a phenomenological description of the internal field.[15] However, because such nonphysical parametrizations cannot provide any insight into the electronic structure of **1**, we refrained from this approach.

In summary, it is possible to fit the broad features of the magnetic, THz-EPR, and magnetic Mössbauer data of **1** with an $S = 1$ SH. This description, however, fails in noticeable details; for example, it leads to inconsistent magnetic hyperfine couplings for the different M_S levels. More importantly, the enormous D, g_{av}, and TIP values, as well as the highly anisotropic **g** matrix and the positive internal fields at the ^{57}Fe nucleus found for **1** hint at the presence of a significant unquenched orbital angular momentum and violation of the preconditions of the SH formalism. This, at least in part, undermines the credence of conclusions about the electronic structure of complex **1** drawn from traditional SH analyses. We must emphasize that, in the present "fortuitous" case, the failure of the SH approach is technically not so obvious because of the limited number of magnetic sublevels in a triplet; however, the failures are significant enough to look for a more physical analysis that is based on the actual electronic structure of the compound, which will be developed below.

3.2. Ab Initio Calculations. In a quest for a more satisfying and physically proper parametrization of the spectroscopic data than the usual SH approach and to gain more fundamental insight into the electronic structure of **1**, we performed detailed ab initio calculations. As specified in the Computational Details section, because of the existence of three different porphyrin conformations,[7] CASSCF(8,11)/NEVPT2 calculations on the ruffled, saddled, and planar porphyrin conformations have been carried out (see the Computational Details for more details on the calculations). Gratifyingly, the calculations delivered the same energetic ordering of the four lowest-lying triplet states irrespective of the core conformations (Table 1), consistent with earlier work.[7,14,15,17] Specifically, the lowest-energy state was predicted to be ^{3}A$_{2g}$, having a leading configuration (90%) of (d$_{xy}$)^2(d$_{z^2}$)^2(d$_{xz,yz}$)^2, and none of the remaining electron configurations has a weight exceeding 1%. A ^{3}E$_g$ state was found approximately 1000 cm^{-1} above ^{3}A$_{2g}$. In addition to the dominant ^{3}E$_g$(A) electron configuration, viz., (d$_{xy}$)^2(d$_{z^2}$)^1(d$_{xz,yz}$)^3, both components of ^{3}E$_g$ contain sizable contributions (10−15%) from the (d$_{xy}$)^1(d$_{z^2}$)^2(d$_{xz,yz}$)^3 electron configuration [^{3}E$_g$(B)]. It is worthwhile to note that the core distortion does not discernibly lift the 2-fold degeneracy of the two ^{3}E$_g$ components, labeled as ^{3}E$_g$(x) and ^{3}E$_g$(y) in Table 1, with the highest splitting of only 20 cm^{-1} found for the saddled core conformation, in agreement with the effective D_{4h} symmetry postulated above. Finally, a ^{3}B$_{2g}$ state with a leading electron configuration of (d$_{xy}$)^1(d$_{z^2}$)^1(d$_{xz,yz}$)^4 (90%) was computed to be situated at much higher energy (>4000 cm^{-1}).

Table 1. Vertical Excitation Energy (cm^{-1}) from the ^{3}A$_{2g}$ Ground State to the Triplet States ^{3}E$_g$(x), ^{3}E$_g$(y), and ^{3}B$_{2g}$ for Different Core Conformations of Complex 1 (Planar, Ruffled, and Saddled) Estimated by CASSCF(8,11)/NEVPT2 Calculations

core conformation	^{3}E$_g$(x)	^{3}E$_g$(y)	^{3}B$_{2g}$
planar	979	997	4934
ruffled	917	920	4758
saddled	835	855	4753

As discussed in the Introduction, the small energy difference between ^{3}A$_{2g}$ and ^{3}E$_g$ is, unfortunately, not decisive because it is within the uncertainty range of the quantum-chemical methods employed. CASSCF calculations typically tend to overestimate excitation energies, and even with the second-order perturbative corrections, such as NEVPT2, errors of a few hundred wavenumbers are not uncommon, even for d−d excited states, where there is a large amount of error cancellation because the electron correlation energies of all states inside the d manifold tend to be quite similar.[47] Thus, the ground state of **1** being either ^{3}A$_{2g}$ or ^{3}E$_g$ cannot be unambiguously assigned on the basis of calculations alone. Nevertheless, the theoretical results strongly suggest that the ^{3}A$_{2g}$ and ^{3}E$_g$ states are energetically well-isolated from other triplet excited states. The energetic proximity of ^{3}A$_{2g}$ and ^{3}E$_g$ indicates the Fe d$_{xz}$, d$_{yz}$, and d$_{z^2}$ orbitals to be of similar energy. More importantly, in the present case, spin−orbit coupling (SOC) is expected to considerably mix the ^{3}A$_{2g}$ and ^{3}E$_g$ states because their energy separation is comparable to the effective SOC constant for Fe(II) (∼400 cm^{-1}).[48] As elaborated on below, such SOC-induced mixing gives rise to the unusual magnetic properties of **1** discussed in section 3.1. In order to

Scheme 2. H_{EH} Matrix (eq 4) on the Basis of the Symmetry-Adapted $|^3E_g,Y\rangle$ and $|^3A_{2g},M_S\rangle$ Magnetic Sublevels[a]

$$
\begin{array}{ccccccccc}
|^3A_{2g},0\rangle & |^3A_{2g},-1\rangle & |^3A_{2g},+1\rangle & |^3E_g,B_1\rangle & |^3E_g,B_2\rangle & |^3E_g,E_-\rangle & |^3E_g,E_+\rangle & |^3E_g,A_1\rangle & |^3E_g,A_2\rangle \\
\hline
0 & 2\mu_B B_- & 2\mu_B B_+ & & & \mu_B C B_- & \mu_B C B_+ & -\frac{\zeta}{\sqrt{2}}C & \\
2\mu_B B_+ & -2\mu_B B_z & & -\frac{\mu_B C B_-}{\sqrt{2}} & \frac{\mu_B C B_-}{\sqrt{2}} & -\frac{\zeta}{2}C & & \frac{\mu_B C B_+}{\sqrt{2}} & -\frac{\mu_B C B_+}{\sqrt{2}} \\
2\mu_B B_- & & +2\mu_B B_z & -\frac{\mu_B C B_+}{\sqrt{2}} & -\frac{\mu_B C B_+}{\sqrt{2}} & & -\frac{\zeta}{2}C & \frac{\mu_B C B_-}{\sqrt{2}} & \frac{\mu_B C B_+}{\sqrt{2}} \\
 & -\frac{\mu_B C B_+}{\sqrt{2}} & -\frac{\mu_B C B_-}{\sqrt{2}} & \Delta_{A-E}-\frac{\zeta}{2}A & 2\mu_B B_z+A\mu_B B_z & -\sqrt{2}\mu_B B_+ & -\sqrt{2}\mu_B B_- & & \\
 & \frac{\mu_B C B_+}{\sqrt{2}} & -\frac{\mu_B C B_-}{\sqrt{2}} & 2\mu_B B_z+A\mu_B B_z & \Delta_{A-E}-\frac{\zeta}{2}A & \sqrt{2}\mu_B B_+ & -\sqrt{2}\mu_B B_- & & \\
\mu_B C B_+ & -\frac{\zeta}{2}C & & -\sqrt{2}\mu_B B_- & \sqrt{2}\mu_B B_- & \Delta_{A-E}-A\mu_B B_z & & \sqrt{2}\mu_B B_+ & \sqrt{2}\mu_B B_+ \\
\mu_B C B_- & & -\frac{\zeta}{2}C & -\sqrt{2}\mu_B B_+ & -\sqrt{2}\mu_B B_+ & & \Delta_{A-E}+A\mu_B B_z & \sqrt{2}\mu_B B_- & -\sqrt{2}\mu_B B_- \\
-\frac{\zeta}{\sqrt{2}}C & \frac{\mu_B C B_-}{\sqrt{2}} & \frac{\mu_B C B_+}{\sqrt{2}} & & & \sqrt{2}\mu_B B_- & \sqrt{2}\mu_B B_+ & \Delta_{A-E}+\frac{\zeta}{2}A & 2\mu_B B_z-A\mu_B B_z \\
 & -\frac{\mu_B C B_-}{\sqrt{2}} & \frac{\mu_B C B_-}{\sqrt{2}} & & & \sqrt{2}\mu_B B_- & -\sqrt{2}\mu_B B_+ & 2\mu_B B_z-A\mu_B B_z & \Delta_{A-E}+\frac{\zeta}{2}A
\end{array}
$$

[a] ^3E_g is the representation of the parent electronic state and Y is the D_4 double-group irreducible representation of the magnetic sublevel (detailed state compositions in terms of the $|^3E_g(x),M_S\rangle$ and $|^3E_g(y),M_S\rangle$ magnetic sublevels described in eqs S4a–S4g). The H_Δ terms are displayed in red. The H_{SOC} terms are displayed in green. The H_{Zee} terms are displayed in brown (spin Zeeman) and blue (orbital Zeeman). For clarity, the zero matrix elements are omitted, and the following substitutions have been used: $A = \cos 2\theta$, $B_\pm = \frac{1}{\sqrt{2}}(B_x \pm iB_y)$, and $C = \sqrt{3}\cos\theta - \sin\theta$. B_x, B_y, and B_z are the three components of the applied magnetic field B_{ext}.

correlate the theoretical results with the experiment, we decided to construct a new EH that explicitly treats SOC and Zeeman interactions of the nine magnetic sublevels arising from the $^3A_{2g}$ and ^3E_g states. Such a treatment allowed us to perform physically justified simulations of the experimental data beyond the conventional SH formalism.

3.3. Simulation of Experimental Data Using an EH Acting on the $^3A_{2g}$ and ^3E_g States.

To set up a parametrized EH for simulation of the magnetic data of complex **1**, we first carried out ligand-field-type analyses. Nonrelativistic many-electron basis functions were constructed from the dominant electronic configurations of the $^3A_{2g}$ and ^3E_g states, using pure Fe d orbitals. In the present case, the covalency effects can be safely neglected because all occupied Fe d orbitals of $^3A_{2g}$ and ^3E_g are essentially nonbonding. By convention, the porphyrin plane was referred to as the *xy* plane, and its normal vector was chosen as the *z* axis. For M_S = +1, the many-electron basis functions are given by

$$|^3A_{2g}, +1\rangle = |d_{xy}\overline{d_{xy}}d_{xz}d_{yz}d_{z^2}\overline{d_{z^2}}| \tag{3}$$

$$|^3E_g^\theta(x), +1\rangle = \cos\theta|^3E_g^\theta A(x), +1\rangle + \sin\theta|^3E_g B(x), +1\rangle \tag{3a}$$

$$|^3E_g^\theta(y), +1\rangle = \cos\theta|^3E_g^\theta A(y), +1\rangle + \sin\theta|^3E_g B(y), +1\rangle \tag{3b}$$

Here, the orbitals with and without an overbar are populated by spin-down and spin-up electrons, respectively, and the brackets |···| denote normalized Slater determinants. As suggested by the CASSCF calculations, a mixing angle (θ) was introduced in eq 3 to describe the mixing of the following two E_g configurations.

$$|^3E_gA(x), +1\rangle = |d_{xy}\overline{d_{xy}}d_{xz}d_{yz}\overline{d_{yz}}d_{z^2}| \tag{3c}$$

$$|^3E_gB(x), +1\rangle = |d_{xy}d_{xz}\overline{d_{xz}}d_{yz}d_{z^2}\overline{d_{z^2}}| \tag{3d}$$

$$|^3E_gA(y), +1\rangle = |d_{xy}\overline{d_{xy}}d_{xz}\overline{d_{xz}}d_{yz}d_{z^2}| \tag{3e}$$

$$|^3E_gB(y), +1\rangle = |d_{xy}d_{xz}d_{yz}\overline{d_{yz}}d_{z^2}\overline{d_{z^2}}| \tag{3f}$$

Similarly, one can write down the basis functions for M_S = 0 and −1. The dimension of the Hilbert space in which the EH is expressed thus amounts to nine.

Magnetometry Measurements. To simulate the SQUID data, the effective electronic Hamiltonian (H_{EH}) consisting essentially of SOC (H_{SOC}) and Zeeman operators (H_{Zee}) was diagonalized on the basis of that described above.

$$\mathbf{H}_{EH} = H_\Delta + H_{SOC} + H_{Zee} \tag{4}$$

$$H_\Delta = E(X)\delta_{X,M_{S'}}\delta_{M_S,M_{S'}} \tag{4a}$$

Here, E(X) corresponds to the energy of the unperturbed states of symmetry representation X [A_{2g}, $E_g(x)$, or $E_g(y)$], and the Kronecker deltas $\delta_{X,X}$ and $\delta_{M_S,M_S'}$ are equal to 1 if the symmetry representation and the M_S values of the unperturbed states in the bra and ket are identical. H_Δ introduces an adjustable energy gap $\Delta_{A-E} = E(^3E_g) - E(^3A_{2g})$ between the $^3A_{2g}$ and ^3E_g states. The matrix elements of H_{SOC} and H_{Zee} on the basis of the nine magnetic sublevels were computed by using the usual single-electron terms.

$$H_{\mathrm{SOC}} = \zeta \sum_{i} \sum_{l=x,y,z} \hat{l}_i(i)\cdot\hat{s}_i(i) \tag{4b}$$

$$H_{\mathrm{Zee}} = \sum_{i} \mu_{\mathrm{B}}[g_{\mathrm{e}}\vec{s}(i) + \vec{l}(i)]\cdot\overrightarrow{B_{\mathrm{ext}}} \tag{4c}$$

ζ is the effective one-electron SOC constant, and g_e, the free electron g value, was fixed at 2.0. The total $\mathbf{H}_{\mathrm{EH}}$ matrix on the basis of the nine magnetic sublevels is shown in Scheme 2. For the Zeeman operator, the matrix elements for the orbital angular momentum $\hat{l}_i$ operators on the real d orbitals are tabulated in the literature,[49] and those for the spin angular momentum $\hat{s}_i$ operating on the spin part of the orbitals were obtained by using the ladder operator technique. Diagonalization of the $\mathbf{H}_{\mathrm{EH}}$ matrix (Scheme 2), which takes into account the SOC of the $^3A_{2g}$ and ^3E_g states as well as their Zeeman interaction with applied fields, yields the nine magnetic sublevels as eigenstates and their energies as eigenvalues. The magnetization (M) and magnetic susceptibility (χ) were directly computed from the resulting energies by using the microscopic magnetization $M_i = -\partial E_i/\partial B_{\mathrm{ext}}$ for the sublevels i and $\chi = M/B_{\mathrm{ext}}$, where M is the molar magnetization.[38]

For simulations of the SQUID data, the energy splitting of the $^3A_{2g}$ and ^3E_g states, $\Delta_{\mathrm{A-E}}$, and the mixing angle θ (eqs 3a and 3b) were defined as two fitting parameters. To avoid overparametrization, splitting of the two E_g components was neglected, consistent with the nearly vanishing splitting delivered by the CASSCF/NEVPT2 calculations (<20 cm^{-1}). In other words, we assumed axial symmetry for **1**, as suggested by the THz-EPR observations (see section 3.1). The SOC constant ζ was fixed to 400 cm^{-1}, a typical value for Fe(II) (400−430 cm^{-1}).[48,49] A satisfactory global fit to all SQUID data yielded $\Delta_{\mathrm{A-E}}$ = 950 cm^{-1} and $\theta = -0.13\pi$ (Figure 4 and Table 2). Of note, unlike the SH simulations, the EH simulations do not require any TIP correction.

The EH simulations with the parameters summarized in Table 2 revealed that the lowest-energy eigenstates of **1** are a triplet with thermally accessible magnetic sublevels $|\phi_0\rangle$, $|\phi_+\rangle$, and $|\phi_-\rangle$. They are energetically reasonably well isolated from the other sublevels by at least 957 cm^{-1} (Figure 5). The triplet is split into a low-lying singlet $|\phi_0\rangle$ and an excited doublet $|\phi_\pm\rangle$ with an energy gap of ΔE = 94 cm^{-1}, a situation similar to a usual triplet with D = 94 cm^{-1} in the SH formalism.

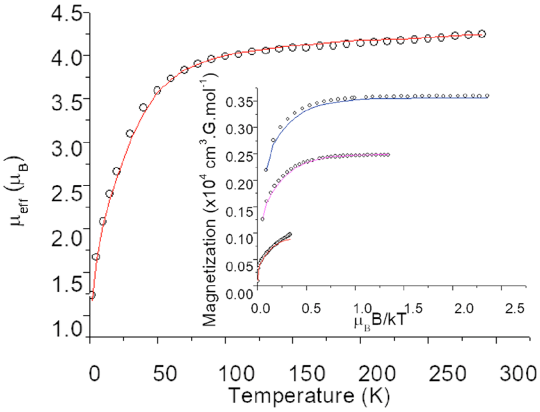

Figure 4. EH simulations of the effective magnetic moment of a powder sample of **1** recorded at different temperatures with a field of 1 T and (inset) isofield magnetization curves under 1 T (red), 4 T (magenta), and 7 T (blue). The dots represent the same experimental data as those shown in Figure 1, and the solid lines represent the best fits obtained with the EH parameters $\Delta_{\mathrm{A-E}}$ = 950 cm^{-1} and θ = -0.13π (eq 4). The simulations take 7.7% impurity into account with S = 2.

Table 2. EH Parameters Used for the Global Simulation of Magnetic Data, Zero-Field THz-EPR Spectra, and Applied-Field Mössbauer Spectra of 1

parameter	meaning	value	comment
$\Delta_{\mathrm{A-E}}$	energy gap of the $^3A_{2g}$ and ^3E_g states	950 cm^{-1}	optimized
θ	mixing angle of the $^3E_g(A)$ and $^3E_g(B)$ configurations	-0.13π	optimized
ζ	effective SOC constant of Fe(II)	400 cm^{-1}	fixed
g_e	spin-only g value	2.0	fixed
$\langle r_d^{-3}\rangle$	d-orbitals r^{-3} expectation value[a]	5.4 a_0^{-3}	optimized
$A_{\mathrm{FC}}/g_{\mathrm{N}}\beta_{\mathrm{N}}$	Fermi contact contribution to HFC[b]	−21.5 T	fixed
δ	Mössbauer isomer shift	0.56 mm/s	fixed[c]
ΔE_{Q}	Mössbauer electric quadrupole splitting	+1.31 mm/s	fixed[c]
η	Mössbauer asymmetry parameter of the EFG tensor, $\eta = (V_{xx} - V_{yy})/V_{zz}$	0	fixed

[a] Used for evaluation of the anisotropic part of the ^{57}Fe hyperfine coupling tensor A only. [b] Isotropic contribution to the ^{57}Fe hyperfine coupling tensor; g_{N} and β_{N} are the nuclear g factor and nuclear magneton, [c] Values taken from the zero-field Mössbauer spectrum; the sign of ΔE_{Q} was taken from the magnetic spectra.

The present approach resembles Maltempo's model used to explain the magnetism of high-spin iron(III) porphyrins.[50] However, in the present case, the unusual magnetic properties of **1** do not originate from the interaction of two states with different spin but rather from the coupling of three different S = 1 states. In fact, we also examined the influence of the low-lying quintet state ($^5A_{1g}$) with a leading electron configuration of $(d_{z^2})^2(d_{xy})^1(d_{x^2-y^2})^1(d_{xz})^1(d_{yz})^1$ (>90%) on the magnetic properties of complex **1**. By enlarging the model space to include it in the EH, no significant changes have been found (for more details, see the Supporting Information), consistent with an earlier work based on ligand-field theory.[7c] Therefore, the quintet state will no longer be considered hereafter.

Applied-Field ^{57}Fe Mössbauer Spectroscopy. To simulate the applied-field ^{57}Fe Mössbauer data, the effective electronic Hamiltonian ($\mathbf{H}_{\mathrm{EH}}$; eq 4) was complemented by the following nuclear Hamiltonian (H_{nuc}):[51]

$$H_{\mathrm{nuc}} = H_\delta + H_{\mathrm{Q}} + H_{\mathrm{Z}} + H_{\mathrm{HFC}} \tag{5}$$

The first term provides the isomer shift, which is just uniformly added to all Mössbauer transition energies, the second and third terms are the usual quadrupole and nuclear Zeeman interactions, as were already given in eqs 2b and 2c, respectively, and the fourth term is the magnetic hyperfine interactions. The last term has three different physical origins, viz., the Fermi contact (H_{FC}), spin-dipole (H_{SD}), and orbital (H_{LI}) contributions.

$$H_{\mathrm{HFC}} = H_{\mathrm{FC}} + H_{\mathrm{SD}} + H_{\mathrm{LI}} \tag{5a}$$

$$H_{\mathrm{FC}} = \mu_{\mathrm{B}}\beta_{\mathrm{N}}g_{\mathrm{e}}g_{\mathrm{N}}\vec{I}\cdot\left[\sum_{i}\frac{8\pi}{3}\delta(r_i)\vec{s}_i\right] = \beta_{\mathrm{N}}g_{\mathrm{N}}A_{\mathrm{FC}}\vec{I}\cdot\vec{S} \tag{5b}$$

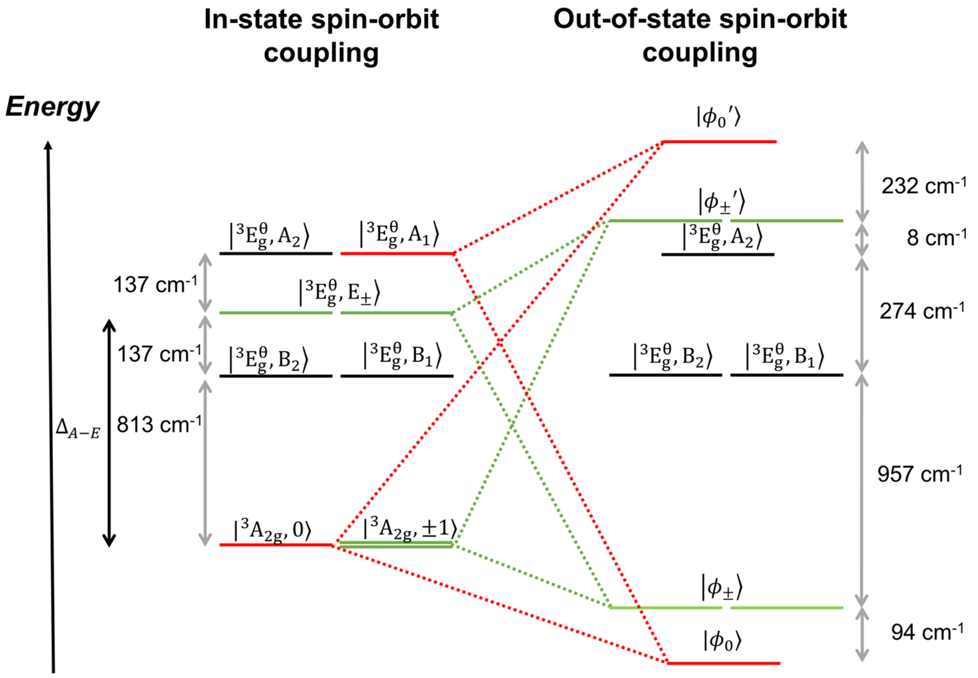

Figure 5. Final energy spectrum of the in-state and out-of-state SOC of the nine magnetic sublevels, computed by using the EH in the absence of any external field. On the left side, the symmetry-adapted states arising from in-state SOC between $|E_g, Y\rangle$ and $|A_{2g}, M_S\rangle$ are shown, and all state compositions are available in the Supporting Information. The dotted lines represent interaction through the out-of-state SOC. On the right side, the states $|\phi_0\rangle$, $|\phi_+\rangle$, $|\phi_-\rangle$, $|\phi_+'\rangle$, $|\phi_-'\rangle$, and $|\phi_0'\rangle$ represent the magnetic sublevels resulting from in-state and out-of-state SOC. The states of A_1 symmetry coupling through out-of-state SOC are shown in red. The states of E symmetry coupling through out-of-state SOC are shown in green. The states that are not coupled through out-of-state SOC are displayed in black.

$$H_{SD} = \mu_B \beta_N g_e g_N \vec{I}\cdot\left[\sum_i \frac{3(\vec{r}_i\cdot\vec{s}_i)\vec{r}_i}{r_i^5} - \frac{\vec{s}_i}{r_i^3}\right] \tag{5c}$$

$$H_{LI} = 2\mu_B \beta_N g_N \vec{I}\cdot\sum_i \frac{\vec{l}_i}{r_i^3} \tag{5d}$$

Here $\delta(r_i)$ is the Dirac delta function, r_i the radius of electron i with respect to the ^{57}Fe nucleus, and A_{FC} a parameter to be determined (see below). Importantly, $\vec{S}$ refers to the real spin angular momentum operator, not to be confused with the pseudospin $\tilde{S}$ of the SH formalism (eqs 1 and 2a).

The following approximations were invoked to compute the magnetic hyperfine interaction, H_{HFC}. First, because, in the presence of external fields larger than a few hundred gauss, the electronic Zeeman interaction is much stronger than all other interactions involving the nuclear spin, the nuclear and electronic states are essentially decoupled. As such, one can replace the electron-spin and orbital angular momenta operators in H_{HFC} by their expectation values and diagonalize the electronic and nuclear Hamiltonians separately. Second, we neglected the anisotropic covalency for different d orbitals by replacing the individual r_i^{-3} operators by a unique expectation value $\langle r_d^{-3}\rangle$ for the Fe d_{xy}, d_{xz}, d_{yz}, and d_{z^2} orbitals.[52] Therefore, the nuclear Hamiltonian can be simplified to

$$\begin{aligned} H_{nuc} &= H_\delta + H_Q - \beta_N g_N \vec{I}\cdot\overrightarrow{B_{eff}} \\ &= H_\delta + H_Q - \beta_N g_N \vec{I}\cdot(\overrightarrow{B_{int}} + \overrightarrow{B_{ext}}) \end{aligned} \tag{5e}$$

where the internal field B_{int} is given by

$$\overrightarrow{B_{int}} = -2\mu_B\langle r_d^{-3}\rangle\langle\vec{L}\rangle - 2\mu_B\langle r_d^{-3}\rangle\left\langle\left[\sum_i \frac{3(\vec{r}_i\cdot\vec{s}_i)\vec{r}_i}{r_i^2} - \vec{s}_i\right]\right\rangle - A_{FC}\langle\vec{S}\rangle \tag{5f}$$

where $\vec{L}$ corresponds to the orbital angular momentum operator. The three terms in eq 5f correspond to the orbital, spin-dipole, and Fermi contact contributions to the internal field: $\overrightarrow{B_{int}^{LI}}$, $\overrightarrow{B_{int}^{SD}}$ and $\overrightarrow{B_{int}^{FC}}$, respectively. Finally, because the experimental spectra showed that the system is in the regime of fast paramagnetic relaxation (section 3.1), the ^{57}Fe nuclei in the sample do not experience an individual internal field for each populated magnetic sublevel but a thermally averaged internal field given by

$$\langle\overrightarrow{B_{int}}\rangle = \frac{\sum \overrightarrow{B_{int_i}}\, e^{-E_i/k_BT}}{\sum e^{-E_i/k_BT}} \tag{5g}$$

where E_i is the energy of the magnetic sublevel i, k_B the Boltzmann constant, and T the temperature.

To simulate the ^{57}Fe Mössbauer data, the expectation values of the electronic operators involved in eq 5f were directly calculated by diagonalization of H_{EH} with the parameters determined by the magnetometry investigations (Figure 6). Furthermore, the isomer shift and quadrupole splitting were fixed to the values obtained by the zero-field ^{57}Fe Mössbauer measurements. However, neither $\langle r_d^{-3}\rangle$ nor the Fermi contact contribution A_{FC} can be calculated within the approximations inherent to this EH, and both have to be treated as fitting parameters. To complicate matters, because $\langle r_d^{-3}\rangle$ and A_{FC} are covariant, a unique fit could not be found. To circumvent this problem, the value of A_{FC} was fixed to 21.5 T, according to the

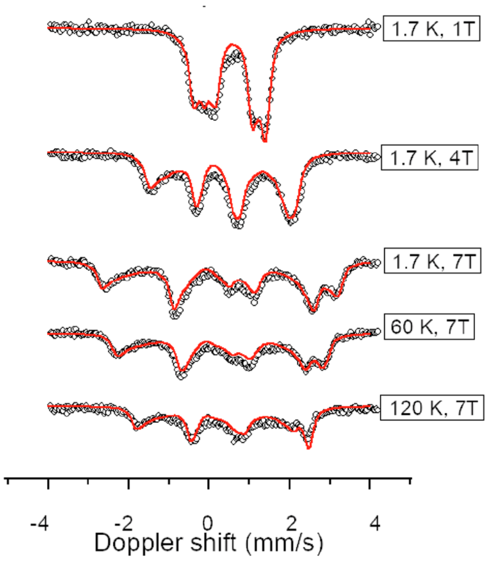

Figure 6. Applied-field ^{57}Fe Mössbauer spectra of a powder sample of **1** recorded at different temperatures, from top to bottom: $B_{\text{ext}} = 1$ T, $T = 1.7$ K; 4 T, 1.7 K; 7 T, 1.7 K; 7 T, 60 K; 7 T, 120 K. The dots represent the same experimental measurements as those shown in Figure 3, and the solid lines represent the best fits obtained from the simulation using the EH and HFC expressions of eqs 4 and 5 with the parameters summarized in Table 2.

empirical rule that the Fermi contact contributions is 21−22 T per unit spin for most ferric and ferrous complexes.[53] The remaining parameter $\langle r_d^{-3}\rangle$ was allowed to vary freely during the simulation, and *all* VTVH ^{57}Fe Mössbauer spectra can be satisfactorily simulated with $\langle r_d^{-3}\rangle = 5.4\ a_0^{-3}$. This value is similar to that found for the metallic Fe ($5.5\ a_0^{-3}$),[49] thereby indicating that expansion of the Fe electron density arising from the ligand field counteracts its contraction because of the higher oxidation state of the Fe center in complex **1**.

In summary, *all* magnetometry and magnetic Mössbauer data of **1** could be fitted with the same EH as that shown in Figures 4 and 6. It should be emphasized that the EH is physically transparent and has only three adjustable parameters, i.e., the energy difference between the ^3E_g and $^3A_{2g}$ states (Δ_{A-E}) and the relative weights of the $^3E_g(A)$ and $^3E_g(B)$ configurations controlled by the angle θ; in addition, for magnetic hyperfine coupling calculations, only the $\langle r_d^{-3}\rangle$ expectation value of the d orbitals has to be considered. The success of the EH is based on the theoretical findings that $^3A_{2g}$ and ^3E_g are well-isolated from other triplet states, and their marginal energy splitting is commensurate with the effective SOC constant of Fe(II) (~400 cm^{-1}). To explicitly treat the SOC of $^3A_{2g}$ and ^3E_g, the EH was designed to deliberately act on the nine-dimensional Hilbert space spanned by them only. In an earlier investigation reported by Mitra and co-workers[7c] to simulate the magnetic data of **1**, a model derived from the ligand-field theory is proposed that involves three parameters representing the energies of the d_{z^2}, d_{xy}, and $d_{x^2-y^2}$ orbitals relative to $d_{xz,yz}$ but requires a basis dimension of as large as 160. The complexity of the ligand-field model largely foiled attempts to pinpoint the underlying electronic-structure features that are responsible for the complex experimental observations. The computational prescreening used in the present work renders our EH as probably the simplest viable solution to the problem.

3.4. Origin of the Unusual Magnetic Properties.

Parametrization of the electronic structure of **1** derived from EH analyses of its magnetic and Mössbauer properties is elegant and physically very satisfying because it deals just with energy splitting and quantum-chemical mixing of the most important electronic states of the compound. In fact, these parameters yield immediate chemical information about the ligand-field splitting of the valence orbitals of Fe. However, deduction of the magnetic properties from the EH parameters is complex and rather tedious, in contrast to SH descriptions, in general, the eight parameters of which (D, E/D, full $\mathbf{g}$ matrix) directly reflect the magnetic properties of the ground state, such as the energy splitting of the magnetic levels and their Zeeman effect. In order to analyze the relationship of the SH and EH treatments in more depth, we will derive in the following the magnetic and hyperfine properties of **1** in terms of the SH parameters from the EH. This elucidates the origin of the unusual magnetic properties of **1** and also unveils the limitations of the SH formalism.

SOC and ZFS. EH analysis of the magnetic data of **1** revealed a low-lying triplet that is separated from other excited states by >900 cm^{-1} and split into a low-lying singlet sublevel ($|\phi_0\rangle$) and a degenerate doublet ($|\phi_\pm\rangle$; Figure 5). The energy gap $\Delta E = 94$ cm^{-1} within the triplet is equivalent to D in the SH formalism. For transition-metal complexes, ZFS arises primarily from SOC between the ground and low-lying excited states.[54] The orbitally nondegenerate $^3A_{2g}$ state has no first-order SOC, whereas the ^3E_g states possess unquenched orbital angular momentum along the z direction, leading to the first-order SOC within the two components of ^3E_g. Hereafter, we first consider the in-state SOC of ^3E_g and then deal with the out-of-state SOC between the $^3A_{2g}$ and ^3E_g states (the second- and higher-order SOC).

Diagonalization of the SOC matrix of the six magnetic sublevels of ^3E_g yields three non-Kramers doublets labeled as $|^3E_g^\theta, M_S, \pm\rangle$ ($M_S = \pm1, 0$). They are also the eigenfunctions of L_z with the eigenvalues given by

$$\begin{aligned}\langle {}^3E_g^\theta, M_S, \pm|L_z|{}^3E_g^\theta, M_S, \pm\rangle &= \pm(\cos^2\theta - \sin^2\theta)\\ &= \pm\cos 2\theta\end{aligned}\qquad(6)$$

Although, in general, SOC of the molecules does not follow the Russel−Sanders scheme, in the present case, the energies of the three doublets of ^3E_g can be readily computed by their S_z and L_z eigenvalues:

$$E = \Delta_{A-E} \mp \frac{\zeta}{2}M_S\cos 2\theta = \Delta_{A-E} - \frac{\zeta}{2}M_S\langle L_z\rangle \qquad(7)$$

In fact, the six magnetic sublevels of ^3E_g belong to the E, A_1, A_2, B_1, and B_2 irreducible representations in the D_4 double group; therefore, only one of the three doublets is indeed degenerate by symmetry. Specifically, the upper and lower doublets are accidentally degenerate and transform as A_1 and A_2 and as B_1 and B_2, respectively, and the middle one belongs to E (Figure 5, left). The symmetry-adapted states are linear combinations of $|E_g, M_S, \pm\rangle$ and are labeled as $|E_g, Y\rangle$, where Y corresponds to the D_4 double-group irreducible representation of a given state. All state compositions are summarized in the Supporting Information. The three magnetic sublevels of $^3A_{2g}$ transform as E ($M_S = \pm1$) and A_1 ($M_S = 0$) in the D_4 double group and remain degenerate in the first-order SOC treatment.

The degeneracy is lifted by the second-order SOC, for which the states that belong to the same irreducible representation of the D_4 double group can interact with each other, thereby giving rise to the ZFS within the low-lying triplet (Figure 5).

Hereafter, we employed the second-order perturbation theory to estimate the energy gap ΔE between the ground singlet ($|\phi_0\rangle$) and upper doublet ($|\phi_\pm\rangle$). Clearly, because of the close proximity of the A_{2g} and ^3E_g states, the second-order perturbation treatment cannot give an accurate ΔE value but can provide insight into its physical origin. The energy changes ($E^{(2)}$) for each magnetic sublevel of $^3A_{2g}$ due to SOC estimated by second-order perturbation theory are given by

$$E^{(2)}(|^3A_{2g}, 0\rangle) = \frac{|\langle ^3A_{2g}, 0|H_{SOC}|^3E_g^\theta, A_1\rangle|^2}{\Delta_{A-E} + \frac{\zeta}{2}\cos 2\theta} \tag{7a}$$

$$E^{(2)}(|^3A_{2g}, \pm 1\rangle) = \frac{|\langle ^3A_{2g}, \pm 1|H_{SOC}|^3E_g^\theta, E_\pm\rangle|^2}{\Delta_{A-E}} \tag{7b}$$

Therefore, the relationship holds

$$\Delta E \approx E^{(2)}(|^3A_{2g}, \pm 1\rangle) - E^{(2)}(|^3A_{2g}, 0\rangle) \tag{7c}$$

In the present case, the coupling element $|\langle ^3A_{2g}, 0|H_{SOC}|^3E_g^\theta, A_1\rangle|^2 = 1.97\zeta^2$ was found to be twice as large as $|\langle ^3A_{2g}, \pm 1|H_{SOC}|^3E_g^\theta, E_\pm\rangle|^2 = 0.99\zeta^2$ and $|\Delta_{A-E}| \gg \zeta/2$. Finally, $E^{(2)}(|^3A_{2g},0\rangle)$ and $E^{(2)}(|^3A_{2g}, \pm 1\rangle)$ equal to −291 and −167 cm^{-1}, respectively, and ΔE = 124 cm^{-1}. As expected, the estimated energy separation is slightly higher than that determined experimentally. However, this analysis clearly discloses that the large axial ZFS of complex **1** stems from the strong SOC between $^3A_{2g}$ and ^3E_g due to their low-energy separation (950 cm^{-1}).

For the same reason, $^3A_{2g}$ and ^3E_g are heavily mixed by SOC in the three low-lying magnetic sublevels, and their wave functions are of multiconfigurational nature. Indeed, our EH analyses showed that the wave functions of $|\phi_\pm\rangle$ and $|\phi_0\rangle$ contain 12% and 15% contributions from the ^3E_g state, respectively. The state composition of the low-lying triplet is given by

$$\begin{aligned}|\phi_0\rangle &= 0.92|^3A_{2g}, 0\rangle + 0.39|^3E_g^\theta, A_1\rangle \\ &= 0.92|^3A_{2g}, 0\rangle + 0.27(|^3E_g^\theta, +1, -\rangle - |^3E_g^\theta, -1, +\rangle)\end{aligned} \tag{8a}$$

$$\begin{aligned}|\phi_\pm\rangle &= 0.94|^3A_{2g}, \pm 1\rangle + 0.34|^3E_g^\theta, E_\pm\rangle \\ &= 0.94|^3A_{2g}, \pm 1\rangle \mp 0.34|^3E_g^\theta, 0, \pm\rangle\end{aligned} \tag{8b}$$

As elaborated on below, the multiconfigurational nature of the low-lying triplet is the orgin of the peculiar magnetic properties observed for **1**.

Effective Magnetic Moment and g Values. In the SH formalism for powder samples, μ_{eff} at high temperatures is proportional to g_{av}. In fact, besides the TIP contribution to χ, the significant deviation of g_{av} from the g_e value (~2) is responsible in large part for the unusually large μ_{eff} of **1** at high temperature. Hence, to understand the origin of μ_{eff}, it is convenient to extract the g factors from the EH analyses.

Because of the effective D_{4h} symmetry, the $g_{\parallel}$ axis should be along the z direction and $g_\perp$ in the xy plane; i.e., the principal axis of the **g** matrix coincides with the reference frame of the EH. Therefore, by mapping of the matrix elements of the Zeeman operator in the $\tilde{S} = 1$ SH and those in the EH on the basis of $|\phi_0\rangle$ and $|\phi_\pm\rangle$, the principal g values can be directly computed by

$$g_{\parallel} = |\langle\phi_+|g_e\hat{S}_z + \hat{L}_z|\phi_+\rangle| \tag{9a}$$

$$g_\perp = \sqrt{2}|\langle\phi_+|g_e\hat{S}_x + \hat{L}_x|\phi_0\rangle| \tag{9b}$$

This yields $g_{\parallel}$ = 1.85, $g_\perp$ = 3.05, and g_{av} = 2.70, in reasonable agreement with those (1.70, 3.07, 2.70) determined by the SH simulations. (For more details of this analysis using the method proposed by Chibotaru and Ungur,[55] see the Supporting Information.)

For the $g_{\parallel}$ component, the contributions from the spin ($g_{S,\parallel}$) and orbital angular momentum ($g_{L,\parallel}$) are 1.77 and 0.08, respectively. Because the g value (1.0) for orbital angular momenta is only half that for spin angular momenta (2.0), $g_{\parallel}$ is slightly less than 2. For fields in the x/y directions, the g values are $g_{S,\perp}$ = 1.91 and $g_{L,\perp}$ = 1.14. The very large $g_{L,\perp}$ value originates from the substantial unquenched transverse orbital angular momentum of the low-lying triplet, $\langle\phi_0|\hat{L}_x|\phi_\pm\rangle = 0.80$ and $\langle\phi_0|\hat{L}_y|\phi_\pm\rangle = \pm 0.80i$. Ultimately, this should be traced back to the considerable mixing of $^3A_{2g}$ and ^3E_g in the low-lying triplet because in essence $g_{L,\perp}$ stems from the sizable matrix elements of

$$\langle ^3A_{2g}, M_S|\hat{L}_x|^3E_g^\theta, M_S, \pm\rangle = \mp 1.40 \tag{10a}$$

$$\langle ^3A_{2g}, M_S|\hat{L}_y|^3E_g^\theta, M_S, \pm\rangle = -1.40i \tag{10b}$$

Consequently, $g_\perp$ reaches such a large value of 3. Given that $g_{\parallel}$ is less than 2, it is $g_\perp$ = 3.05 that is responsible for the determined effective magnetic moment being significantly higher than the spin-only value for a triplet system.

To gain further insight into the magnetic properties of complex **1**, we also computed microscopic longitudinal ($\mu_{\parallel}$) and transverse ($\mu_\perp$) magnetic moments of the low-lying triplet as a function of the external field. As shown in Figure 7, the ground singlet, $|\phi_0\rangle$, is nonmagnetic along the z direction. This is because $|\phi_0\rangle$ comprises, besides $|^3A_{2g},0\rangle$, which is nonmagnetic, an equal amount of $|^3E_g^\theta,-1,+\rangle$ and $|^3E_g^\theta,+1,-\rangle$. Thus, spin and orbital angular momenta exactly cancel out for field quantitation along the z direction. By contrast, the upper doublet ($|\phi_\pm\rangle$) has sizable spin and orbital angular momenta along the z direction, the latter of which originates from its ^3E_g component ($|^3E_g^\theta,0,\pm\rangle$). When the field is applied in the xy plane, the Zeeman interaction causes mixing of $|\phi_\pm\rangle$ into $|\phi_0\rangle$, yielding the new, field-dependent eigenstates $|\tilde{\phi}_\pm\rangle$ and $|\tilde{\phi}_0\rangle$. Despite the large ZFS between $|\phi_\pm\rangle$ and $|\phi_0\rangle$ of 94 cm^{-1}, such mixing makes the ground sublevel $|\tilde{\phi}_0\rangle$ acquire substantial spin and orbital angular momenta in the xy plane because the transverse spin and orbital angular momenta are proportional to $^1/_2\, g_{S,\perp}$ and $g_{L,\perp}$, respectively. For the upper doublet $|\tilde{\phi}_\pm\rangle$, one of the levels becomes essentially nonmagnetic for fields in the xy plane, whereas the other gains a negative magnetic moment. As such, at low temperatures, complex **1** with exclusive population of the sublevel $|\tilde{\phi}_0\rangle$ features easy-plane magnetization. At first glance, the present situation closely resembles that of the usual $\tilde{S} = 1$ systems with large positive D values, but it should be noted that 38% of $\mu_\perp$ of complex **1** arises from the orbital angular momentum (Table 3). Furthermore, the EH also nicely reproduced the single-crystal

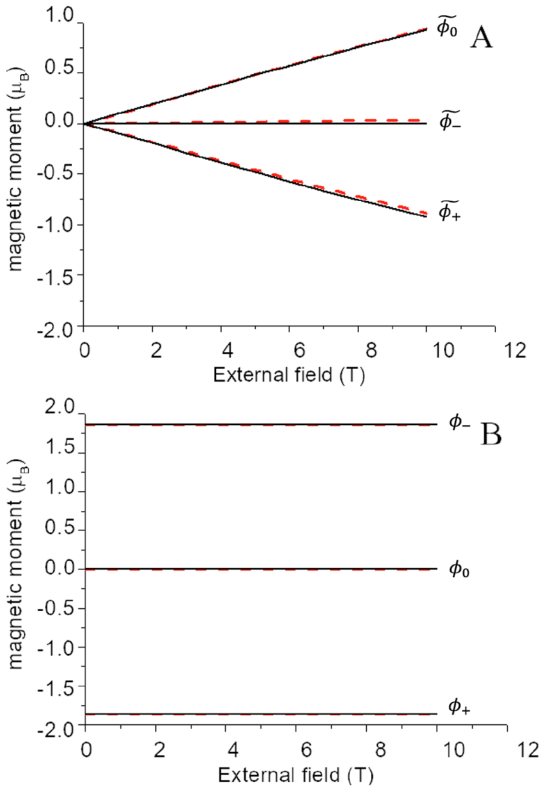

Figure 7. Microscopic transverse (A) and longitudinal (B) magnetic moments of the low-lying triplet as a function of the applied field computed by the EH (red dashed line) with $\Delta_{A-E} = 950$ cm^{-1} and $\theta = -0.13\pi$ and by the SH (black solid line) with $D = 94$ cm^{-1}, $g_{\parallel} = 1.85$, and $g_{\perp} = 3.05$.

susceptibility data of complex **1** reported by Mitra and coworkers,[7c] which show a large transverse magnetic susceptibility ($\chi_{\perp}$) and a vanishing longitudinal one ($\chi_{\parallel}$) below 50 K (Figure S6).

Hyperfine Coupling and Internal Field. In the SH formalism, the internal field is proportional to the hyperfine coupling matrix **A**. Hence, to understand the physical origin of the internal field, one has to extract the **A** matrix from the EH model. For symmetry reasons, the $A_{\parallel}$ axis should be along the z direction and the $A_{\perp}$ axis in the xy plane. By mapping the matrix elements of the SH internal field operators and those of the EH (for more details, see the Supporting Information), the **A** matrix can be computed by

$$\frac{A_{\parallel}}{g_N\beta_N} = |\langle\phi_+|\overrightarrow{B_{\text{int},z}}|\phi_+\rangle| \tag{11a}$$

$$\frac{A_{\perp}}{g_N\beta_N} = \sqrt{2}\,|\langle\phi_0|\overrightarrow{B_{\text{int},x}}|\phi_+\rangle| \tag{11b}$$

The resulting A values and corresponding Fermi contact (A_{FC}), spin-dipole (A_{SD}), and orbital (A_L) contributions are summarized in Table 4. The $A_{\perp}$ value by far surpasses $A_{\parallel}$ but is slightly lower than that deduced from SH simulations for the reasons discussed below. The large and positive $A_{\perp}$ arises from the overwhelming orbital contribution ($A_{L,\perp}$), which even overrides the otherwise predominant negative Fermi contact term ($A_{FC,\perp}$). As elaborated on elsewhere,[56] $A_{L,\perp}$ is proportional to $g_{L,\perp}$; therefore, like $g_{\perp}$, the large $A_{\perp}$ value also originates from the unquenched orbital angular momentum of the low-lying triplet of complex **1**. The anisotropic Fermi contact contribution ($A_{FC,\parallel}$ vs $A_{FC,\perp}$) reflects the significant anisotropy of the g_S values because $A_{FC,\parallel}$ and $A_{FC,\perp}$ are proportional to $g_{S,\parallel}$ and $g_{S,\perp}$, respectively.[56] Of note, this intriguing situation has been experimentally identified for Co(II) and U(IV) complexes,[57] which feature very strong SOC similar to the present case. In the present case, $A_{FC,\parallel}$ and $A_{FC,\perp}$ are also lower than the expected 21.5 T because $g_{S,\parallel}$ and $g_{S,\perp}$ are both lower than 2.0. Finally, the unpaired electrons of **1** are primarily located in the Fe d_{xz}, d_{yz}, and d_{z^2} orbitals, and they all have positive spin-dipole contributions (A_{SD}) along the z direction, which leads to a positive longitudinal component ($A_{SD,\parallel}$) and a negative transverse component ($A_{SD,\perp}$).

Table 4. Extracted SH A Values and Decomposition into Fermi Contact (A_{FC}), Spin-Dipole (A_{SD}), and Orbital (A_L) Contributions, Given in Tesla ($\cong A/g_N\beta_N$)

	total	A_{FC}	A_{SD}	A_L
$A_{\parallel}$	4.6	−19.0	18.2	5.4
$A_{\perp}$	47.5	−20.6	−8.8	76.9

As shown in Table 5, at the base temperature in the presence of an external field of 7 T along the x direction, the ^{57}Fe nucleus of complex **1** experiences a positive transverse field of +10.6 T because of the dominating orbital component originating from $|\tilde{\phi}_0\rangle$. Because this internal field adds to the applied external field, the actual nuclear Zeeman interaction easily surpasses the moderate quadrupole splitting (+1.31 mm/s). As a consequence, the applied-field ^{57}Fe Mössbauer spectrum exhibits a well-resolved six-line pattern (Figure 6). At elevated temperatures, the population of the upper doublet slightly reduces the transverse internal field because of the lower $\mu_{\perp}$ value of $|\tilde{\phi}_{\pm}\rangle$ (Figure 7). Furthermore, the internal field in the xy plane is always much higher than that along the z direction. Such a behavior is not unusual for a system featuring strong easy-plane magnetization, but it should be emphasized that, in the present case, the situation gets accentuated because of $g_{\perp} \gg g_{\parallel}$ and $A_{\perp} \gg A_{\parallel}$.

Limitations of the SH Formalism. In the SH formalism, the field-induced second-order Zeeman coupling between the ground triplet and excited states is completely neglected. In fact, such interactions stabilize all magnetic sublevels of the

Table 3. Expectation Values for the Spin and Orbital Angular Momenta ($\hbar$) and Total Magnetic Moments (μ_B) ($\langle\mu_i\rangle = -(\langle L_i\rangle + g_e\langle S_i\rangle)$) for the Three Low-Lying Magnetic Sublevels of 1 Obtained by Diagonalization the 9 × 9 Matrix of H_{EH} (Eq 4) with Parameters $\Delta_{A-E} = 950$ cm^{-1}, $\theta = -0.13\pi$, and $B = 7$ T Applied along the x and z Directions, Respectively

state	$\langle S_{\perp}\rangle$	$\langle L_{\perp}\rangle$	$\langle\mu_{\perp}\rangle$	state	$\langle S_{\parallel}\rangle$	$\langle L_{\parallel}\rangle$	$\langle\mu_{\parallel}\rangle$
$|\tilde{\phi}_0\rangle$	−0.20	−0.25	0.65	$|\phi_0\rangle$	0	0	0
$|\tilde{\phi}_-\rangle$	0	−0.03	0.03	$|\phi_-\rangle$	−0.885	−0.08	1.85
$|\tilde{\phi}_+\rangle$	0.20	0.22	−0.62	$|\phi_+\rangle$	0.885	0.08	−1.85

Table 5. Decomposition of the Fermi Contact, Spin-Dipole, and Orbital Contributions of the *x* and *z* Components of the Internal Field at Temperatures of 1.7 and 60 K under an External Field of 7 T along the *x* and *z* Directions, Respectively

temperature (K)	internal field	total internal field (T)	Fermi contact contribution (T)	spin-dipole contribution (T)	orbital contribution (T)
1.7	$B_{\mathrm{int},\parallel}$	0	0	0	0
	$B_{\mathrm{int},\perp}$	10.6	−4.3	−1.8	16.7
60	$B_{\mathrm{int},\parallel}$	0.1	−0.5	0.5	0.1
	$B_{\mathrm{int},\perp}$	8.3	−3.2	−1.3	12.8

low-lying triplet and thus raise their magnetic moments. As a consequence, the trace of the $\mu_\perp$ matrix on the basis of this triplet differs from zero. However, in the SH formalism, the trace of the Zeeman matrix is dictated by definition to be zero; hence, these effects cannot be properly described. More importantly, as shown in Figure 7, in the present case, the coupling is state-specific, i.e., the ground singlet ($|\phi_0\rangle$) and upper doublet ($|\phi_\pm\rangle$) interact with distinct excited states through the transverse *orbital* Zeeman interaction. Therefore, for the different magnetic sublevels of the low-lying triplet, the change of the magnetic moment is not identical (more detailed analyses are available in the Supporting Information). The increment for the upper doublet is larger than that for the ground singlet because of the energetic proximity (Table 6).

Table 6. Comparison of the Transverse Magnetic Moments in Units of μ_B and the Internal Mössbauer Fields in Tesla in the *xy* Plane of the Low-Lying Triplet Sublevels with an External Field of 7 T Applied in the *x* Direction and Computed by the SH with D = 94 cm^{-1}, $g_\parallel$ = 1.85, $g_\perp$ = 3.05, $A_\parallel/g_N\beta_N$ = 4.6 T, and $A_\perp/g_N\beta_N$ = 47.5 T and by the EH with Δ_{A-E} = 950 cm^{-1}, θ = −0.13π, and $\langle r_d^{-3}\rangle$ = 5.4 a_0^{-3}

average observable	magnetic sublevel	SH	EH
$\langle\mu_\perp\rangle$	$|\tilde{\phi}_0\rangle$	0.64	0.65
$\langle\mu_\perp\rangle$	$|\tilde{\phi}_-\rangle$	0.0	0.03
$\langle\mu_\perp\rangle$	$|\tilde{\phi}_+\rangle$	−0.64	−0.62
$B_{\mathrm{int},\perp}$	$|\tilde{\phi}_0\rangle$	9.8	10.6
$B_{\mathrm{int},\perp}$	$|\tilde{\phi}_-\rangle$	0	1.4
$B_{\mathrm{int},\perp}$	$|\tilde{\phi}_+\rangle$	−9.8	−8.6

In usual practices to simulate magnetic data, second-order Zeeman effects are typically accounted for by invoking a unique, nonspecific TIP correction to χ. However, here the dominant second-order Zeeman coupling is realized only via transverse orbital angular momentum operators, as shown in Figure 8. Hence, $\mu_\parallel$ remains unaltered, and the induced magnetic moments for $\mu_\perp$ are 0.01, 0.03, and 0.02 μ_B for $|\tilde{\phi}_0\rangle$, $|\tilde{\phi}_-\rangle$, and $|\tilde{\phi}_+\rangle$, respectively (Table 6). The negligible changes in $\mu_\perp$, therefore, render the thermally averaged susceptibility correction almost independent of temperature (Figure S7).

Different from $\mu_\perp$, where the orbital contribution ($\mu_B\langle L_\perp\rangle$) makes a mere 38% of the total magnetic moment, the orbital contribution to the transverse internal field $B^{\mathrm{LI}}_{\mathrm{int},\perp}$ (first term of the sum in eq 5f) accounts for 160% of the overall transverse internal field $B_{\mathrm{int},\perp}$ (eq 5f and Table 5). Hence, unlike for the magnetic moment, dominated by its *spin* contribution, the neglect of transverse *orbital* Zeeman interactions translates into a drastic underestimation of the transverse internal field because the latter is dominated by its *orbital* contribution. As shown in Table 6, inclusion of the second-order orbital Zeeman coupling translates into increases of 0.8, 1.4, and 1.2 T in $B_{\mathrm{int},\perp}$ for $|\tilde{\phi}_0\rangle$, $|\tilde{\phi}_-\rangle$, and $|\tilde{\phi}_+\rangle$, respectively. As a result, the internal field estimated by the SH with the parameters extracted from the EH is inevitably lower than that directly calculated by the EH (Figure 9) because the former treatment neglects the second-order Zeeman interactions. Therefore, in order for the SH to reach the same magnitude of the magnetic splitting in applied-field ^{57}Fe Mössbauer spectra, a larger $A_\perp$ value should be required (Figure 3). This is why $A_\perp$ (50.0 T) determined by the SH simulations of the 1, 4, and 7 T/1.7 K ^{57}Fe Mössbauer spectra considerably exceeds that (47.5 T) extracted from the EH. Despite this, the SH simulations with the same $A_\perp$ value of 50.0 T still underestimate the magnetic splitting of the 7 T ^{57}Fe Mössbauer spectra measured at 60 and

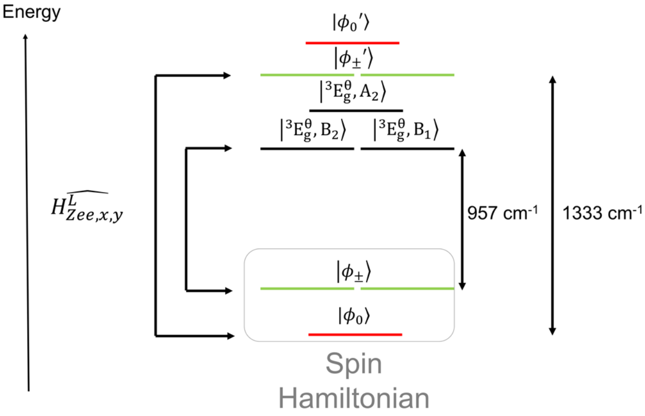

Figure 8. Representation of the second-order Zeeman coupling of the ground triplet with the excited magnetic sublevels after in-state and out-of-state SOC. The color code is the same as that used for Figure 5. The black arrows on the left side represent the *x* and *y* components of the orbital Zeeman coupling between the magnetic sublevels. The states $|\phi_\pm\rangle$ (green) interact with the states $|^3E_g^\theta,B_1\rangle$ and $|^3E_g^\theta,B_2\rangle$; the state $|\phi_0\rangle$ (red) interacts with the state $|\phi_\pm'\rangle$.

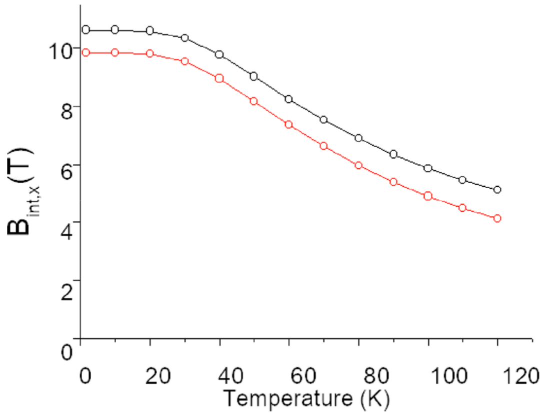

Figure 9. Fast relaxation regime internal field of **1** in the *xy* plane under an external field of 7 T calculated by the SH (red) with D = 94 cm^{-1}, $g_\parallel$ = 1.85, $g_\perp$ = 3.05, and $A_\perp/g_N\beta_N$ = 47.5 and by the EH (black) with Δ_{A-E} = 950 cm^{-1}, θ = −0.13π, and $\langle r_d^{-3}\rangle$ = 5.4 a_0^{-3}.

120 K (Figure 3) because the corrections to the internal field for the upper doublet are larger than those for the ground singlet, and the internal field for the former remains underestimated.

The above study underlines the shortcomings of the SH formalism to describe near-degenerate systems like **1**. The neglect of field-induced coupling between the low-lying triplet and higher-lying states renders the SH unphysical. Because in the present case the second-order Zeeman couplings are small, the SH may provide satisfying simulations at first glance. This is due to the fact that some of the system's features are hidden from spectroscopic measurements; for instance, the poor description of the upper doublet does not deteriorate the quality of the fits of low-temperature applied-field Mössbauer spectra. As shown in Figure 7, if one neglects the minor corrections arising from the second-order Zeeman effects, all other Zeeman couplings within the low-lying triplet can be reasonably parametrized by two factors ($g_{\parallel}$ and $g_{\perp}$). Similarly, because of the effective D_{4h} symmetry of **1**, two of the three low-lying magnetic sublevels of **1** are degenerate; hence, only one SH parameter (D) is adequate to describe the ZFS of its low-lying triplet. This explains why the SH can be fortuitously applied to analyze most spectroscopic data of **1** except those closely relevant to the second-order Zeeman coupling. The present situation is no more than two points determining a straight line. Even so, the phenomenological SH parameters do not shed much light on the physical origin of the experimental observables, which warrants further theoretical interpretations.

3.5. What Is the Appropriate Electronic-Structure Description of the Triplet Ground State of Complex 1?

As elaborated above, all peculiar magnetic properties observed for complex **1** are, in fact, the manifestations of its low-lying triplet featuring strong easy-plane anisotropy at low temperatures, which arises from the existence of substantial unquenched orbital angular momentum in the xy plane for the low-lying singlet sublevel $|\tilde{\phi}_0\rangle$ (according to $D \gg 0$, $E/D = 0$, and $g_{\parallel} \ll g_{\perp}$). This ultimately can be rooted back to mixing of ^3E_g into the closely spaced $^3A_{2g}$ state induced by SOC. In other words, complex **1** is best viewed as having an almost triple degeneracy of the lowest three electronic states that is not dictated by symmetry. If the ground state were best described as a proper triplet of $^3A_{2g}$, complex **1** would not have significant unquenched orbital angular momentum. If the ground state were the doubly degenerate ^3E_g state, complex **1** would exhibit uniaxial magnetic properties because the thus-generated unquenched orbital angular momentum would be oriented along only one rather than two directions.

In the language of theoretical chemistry, our detailed analyses reveal that the electronic ground state of complex **1** is of bona fide multiconfigurational character. In the present context, a configuration is interpreted as an occupation-number vector, with individual orbital occupations being either 0, 1, or 2. The situation is distinctly different from multideterminantal states, where a linear combination of several Slater determinants is required to satisfy spin-symmetry constraints. Note that in the latter cases all required Slater determinants still belong to the same electron configuration but differ in the spin label, viz., spin-up or spin-down, that is assigned to each electron in a given Slater determinant. In general, multiconfigurational character is frequently attributed to transition-metal complexes; however, the vast majority of them are dominated by a single electron configuration, unless systems feature rather high symmetry where multiplets arise due to the distribution of electrons among symmetry-dictated degenerate orbitals. In this regard, most antiferromagnetically coupled transition-metal oligomers are multideterminantal, instead of multiconfigurational. Although the multiconfigurational nature is often deduced by computations, the extent of configuration mixing is to some extent dependent on the choice of orbitals. In fact, there are very few, if any, cases where an authenticated multiconfigurational nature (with contributions of more than one configuration exceeding, say, 10%) is strongly implied by analysis of the experimental data in conjunction with high-level calculations. We emphasize that the SOC between energetically closely spaced electronic states is the *only* reason for the multiconfigurational ground state in this system. Conventionally, multiconfigurational ground states arise from mixing of several electronic configurations caused by electron correlation. However, in order for two states to effectively mix, they must be of the same symmetry, which is not the case here. However, the SOC couples states of different symmetry (and multiplicity). Under normal circumstances, these mixings are very small. However, in **1**, the SOC-induced multiconfigurational character is exceptionally strong given the close energetic proximity of the $^3A_{2g}$ and ^3E_g components.

3.6. Comparison with Related Systems. To the best of our knowledge, complex **1** represents the first integer spin system that has been irrefutably identified to feature such an intriguing electronic structure. However, accidentally triply degenerate ground states have long been identified experimentally for half-integer spin systems. For instance, type III low-spin ferric heme complexes, $[\mathrm{Fe(TPP)(4\text{-}CNPy)_2}]^+$, $[\mathrm{Fe(TPP)}(t\text{-}\mathrm{BuNC})_2]^+$, and $[\mathrm{Fe(OEP)}(t\text{-}\mathrm{BuNC})_2]^+$ represent archetypical examples.[58] Their nondegenerate electronic ground state with a $(d_{xz,yz})^4(d_{xy})^1$ configuration lies slightly below a doubly degenerate state with a $(d_{xz,yz})^3(d_{xy})^2$ configuration. Using the Taylor model,[58] their energy separation is estimated to be in the range of 100−800 cm^{-1}, which is comparable to the effective one-electron SOC constant of Fe(III) (464 cm^{-1}).[48] As a consequence of their bonding situations in analogy to complex **1**, the complexes also feature strong easy-plane anisotropy. Specifically, $[\mathrm{Fe(TPP)(4\text{-}CNPy)_2}]^+$ exhibits an axial EPR spectrum with $g_{\parallel} \leq 0.92$ and $g_{\perp} \geq 2.62$.[59] $[\mathrm{Fe(TPP)}(t\text{-}\mathrm{BuNC})_2]^+$ and $[\mathrm{Fe(OEP)}(t\text{-}\mathrm{BuNC})_2]^+$ possess $g_{\parallel} = 1.83{-}1.94$, $g_{\perp} = 2.20{-}2.28$, and two positive ^{57}Fe A values in the xy plane.[60] Furthermore, the EPR spectra of $S = {}^1/_2$ $[\mathrm{Co^{II}(TPP)}]$ and $[\mathrm{Co^{II}(OEP)}]$ measured in a variety of solvents and solid matrixes showed $g_{\parallel} = 1.6{-}1.8$ and $g_{\perp} = 3.3{-}3.4$.[61] Earlier ligand-field analyses have attributed this large magnetic anisotropy to the three electronic states, with the electron configurations of $(d_{xy})^2(d_{xz,yz})^4(d_{z^2})^1$ and $(d_{xy})^2(d_{xz,yz})^3(d_{z^2})^2$ being close in energy.[62] Different from the above-mentioned compounds with half-integer spins, the difficulty in exploring the electronic structure of complex **1** lies in the fact that it is an integer spin system and has a huge axial ZFS (~94 cm^{-1}). Therefore, complex **1** is EPR-silent for all commercially available EPR spectrometers, and only employing both SQUID and THz-EPR were we able to determine its $g_{\parallel}$ and $g_{\perp}$ values. Moreover, the large $g_{\perp}$ value is also manifested by a large and positive internal field at the ^{57}Fe nucleus in the xy plane.

In the literature, far more systems featuring orbitally almost doubly degenerate ground states have been reported, especially in the burgeoning field of molecular magnetism. In contrast to the systems whose electronic ground states having nearly triple degeneracy like **1**, they possess unquenched orbital angular momenta only along the *longitudinal* direction (z). Therefore, their low-lying spin manifolds exhibit easy-axis anisotropy ($g_{\parallel} \gg g_{\perp}$). Applied-field Mössbauer studies revealed that ferrous octaethyltetraazaporphyrin[53] and phthalocyanine complexes,[63] both being closely related to **1**, have very large and positive internal fields along one direction, which has been ascribed to their ^3E_g ground state having a hole in the quasi-degenerate Fe d_{xz} and d_{yz} orbitals. Note that certain crystalline forms of ferrous phthalocyanine exhibit distinct magnetic properties, which may suggest different electron configurations.[64] Further representative examples of non-Kramers systems are a range of two-coordinate linear high-spin ferrous complexes.[65] Unlike complex **1**, such systems usually have large negative D values and vanishing rhombicity ($E/D \sim 0$). Consequently, their low-lying non-Kramers doublets can be probed by using X-band EPR, in particular in a parallel detection mode. Typically, they feature an effective g factor of >10, which by far exceeds the spin-only value of 8, and a large and positive internal field along the same direction. Both findings indicate a 2-fold pseudodegenerate ground state with a $(d_{xy},d_{x^2-y^2})^3(d_{xz})^1(d_{yz})^1(d_{z^2})^1$ configuration. A series of planar three-coordinate $S = 2$ Fe(II) complexes, $[LFe^{II}X]^0$ (L = β-diketiminate; X = Cl^-, CH_3^-, $NHTol^-$, and NH^tBu^-), also belong to this category.[66] Type I low-spin ferric heme complexes, often referred to as highly anisotropic low-spin species, serve as typical examples of Kramers systems.[58,67] Their EPR spectra are distinguished by a very high g value of ≥ 3, whereas of the remaining two g factors, at least one is substantially less than 2 and sometimes is even hard to identify. The uniaxial magnetic properties exhibited by such complexes are consistent with their 2-fold degenerate ^2E_g ground states with a $(d_{xy})^2(d_{xz,yz})^3$ configuration. Similarly, a low-coordinate $S = {}^3/_2$ Fe(I) complex, $[LFe^I(HCCPh)]^0$ (L = $HC(C[^tBu]N\text{-}[2,6\text{-diisopropylphenyl}])_2^-$), was found to have a large effective g factor of 8.9, with the other two g components less than 0.3 in the X-band EPR spectra.[68] Note that the maximum effective spin-only g value of quartet spin systems is only 6. Furthermore, applied-field ^{57}Fe Mössbauer measurements revealed that $[LFe^I(HCCPh)]^0$ has a large and positive internal field. On the basis of these findings, its ground state was postulated to have nearly 2-fold degeneracy with a $(d_{z^2},d_{yz})^3(d_{xy})^2(d_{xz})^1(d_{x^2-y^2})^1$ configuration.

3.7. Characteristic Spectroscopic Properties for Systems Featuring Orbitally Almost Doubly or Triply Degenerate Ground States.

For all complexes discussed above, their pseudodegenerate orbitals are more than half-filled. Therefore, the partially unquenched orbital angular momentum induced by SOC aligns approximately along the same direction as the spin angular momentum. This notion can be rationalized as follows. In the extreme situation, orbital angular momenta are completely unquenched, such as atoms with spherical symmetry. The third Hund's rule in atomic physics states that, for more than half-filled degenerate shells, the spin−orbit coupled state with maximum total angular momentum value J lies at the lowest energy, thereby indicating that in the low-lying magnetic sublevels the spin and orbital angular momenta orient roughly along the same direction. As a consequence, the spin and orbital contributions to the total magnetic moment should strengthen each other, and the total g factor must be considerably higher than 2. In the other extreme situation, where systems possess orbitally non-degenerate ground states, the orbital angular momenta of their ground states are almost completely quenched. Under such circumstances, SOC between the ground state and low-lying excited states with the same spin as the ground state partially restores the orbital angular momentum in the ground state, thereby leading to significant g shifts, i.e., differences of the measured g factor relative to the spin-only value (~2). As elaborated on elsewhere,[69] an excitation from a doubly to a singly occupied MO introduces a positive g shift, whereas an excitation from a singly to an unoccupied MO gives a negative g shift. More importantly, the magnitude of the resulting g shift is inversely proportional to the energy difference between the thus-generated excited state and the ground state. In the case of systems having orbitally almost doubly degenerate ground states, excitations between the two quasi-degenerate orbitals lead to one very large g shift. However, for complexes whose electronic ground states possess pseudotriple degeneracy, analogous excitations among three nearly degenerate orbitals result in two g components that substantially exceed $g_e \approx 2$. Taken together, easy-plane anisotropy ($g_{\parallel} \ll g_{\perp}$) can be viewed as the spectroscopic signature of orbitally almost triply degenerate systems with more than half-filled degenerate sets.

How about systems whose quasi-degenerate orbitals are less than half-filled? On the basis of the above discussion, one can predict that complexes whose electronic ground states possess 2- and 3-fold quasi-degeneracy are likely distinguished by one and two g factors that are significantly lower than 2, respectively. Our recent work showed that tetragonal iron(V) nitrido and oxo complexes feature an orbitally almost doubly degenerate ground state with a $(d_{xy})^2(\pi^*)^1$ configuration (π^* denotes the two π-antibonding combinations formed by the Fe $d_{xz/yz}$ and N/O $p_{x/y}$ atomic orbitals).[70] Taking $[Fe^V(N)(TPP)]$ as an example, this unusual electronic structure is manifested by its highly anisotropic near-axial EPR spectrum with g = 1.0, 1.70, and 1.83. The in-depth ligand-field analysis revealed that such systems can be distinguished by $g_{\parallel} < g_{\perp} \leq 2$, and the $g_{\parallel}$ and $g_{\perp}$ values obey a simple relationship of $g_{\perp}^2 + (2 - g_{\parallel})^2 = 4$. Earlier work showed that octahedral $[Ti^{III}(OH_2)_6]^{3+}$ complexes in a titanium−cesium alum $[TiCs(SO_4)_2{\cdot}12H_2O]$ feature a bonding situation analogous to that of complex **1**; weak trigonal distortions lift the triple degeneracy of the T_{2g} ground state of $[Ti^{III}(OH_2)_6]^{3+}$ and yield an orbital singlet slightly below a doublet. Its EPR spectrum exhibits a reversed pattern with $g_{\parallel}$ = 1.25 and $g_{\perp}$ = 1.14,[71] compared to that of $[Fe^V(N)(TPP)]$. Although the g values of $[Ti^{III}(OH_2)_6]^{3+}$ determined in different host lattices and in solution are slightly different because of the varying degree of Jahn−Teller distortions,[72] all of them have the same pattern of $g_{\perp} < g_{\parallel} \leq 2$.[73] This is a characteristic feature of complexes having orbitally almost triply degenerate ground states with less than half-filled pseudodegenerate orbitals.[74] To the best of our knowledge, no integer spin systems that possess similar electronic ground states have been experimentally unambiguously identified. Clearly, further experimental and theoretical work is needed to verify whether the proposed spectroscopic signature is applicable to other systems. Very recently, a square-planar iron(II) corrole complex, $[Fe^{II}(TPC)]^-$ (TPC^{3-} = 5,10,15-triphenylcorrole trianion), has been structurally and spectroscopically characterized to have an $S = 1$ ground state.[75] DFT calculations cannot determine its ground-state electron configurations to be either $(d_{xy})^2(d_{z^2})^2(d_{xz,yz})^2$ or $(d_{xy})^2(d_{z^2})^1(d_{xz,yz})^3$, a situation similar to that encountered for complex **1**.

3.8. Implications of the Electronic Structure of Complex 1 for CO_2 Reduction.

The near-triple degeneracy

of the Fe d_{xz}, d_{yz}, and d_{z^2} orbitals also plays an important role in its catalyzed CO_2 electrochemical reduction. As elaborated on elsewhere,[5] upon reduction two additional electrons successively enter into the TPP lowest unpoccupied MOs (LUMOs) of **1**, which transform as the same irreducible representation, e_g, as the Fe d_{xz} and d_{yz} orbitals in the D_{4h} point group. Consequently, the singlet ground state of dianion $\mathbf{1}^{2-}$ is attained by antiferromagnetic coupling between an intermediate Fe(II) ion with an electron configuration of $(d_{xy})^2(d_{z^2})^2(d_{xz,yz})^2$ and a triplet $TPP^{\bullet\bullet 4-}$ ligand, which is realized by favorable symmetry-allowed interaction of the Fe $d_{xz,yz}$ and TPP e_g magnetic orbitals.[5a] Furthermore, the Fe d_{xz}, d_{yz}, and d_{z^2} orbitals of $\mathbf{1}^{2-}$ should retain a similar triple degeneracy identified for **1** because both complexes feature the same coordination geometry. $[Ni^I(cyclam)]^+$ (cyclam = 1,4,8,11-tetraazacyclotetradecane) featuring an analogous coordination geometry represents another well-known CO_2-to-CO electrocatalyst.[76] Our earlier work revealed that formation of a η^1-CO_2 adduct, which is the first step of the catalytic cycle of CO_2 reduction, is primarily driven by electron donation from the Ni d_{z^2} orbital to the CO_2 π^* LUMO.[77] A similar situation is expected for CO_2 association at $\mathbf{1}^{2-}$. During this process, because of the their triple degeneracy, electron donation from the Fe d_{z^2} orbital likely triggers electron transfer from the TPP e_g orbital to the Fe $d_{xz,yz}$ orbitals; consequently, the electron density of the Fe center is largely intact. Without such an electron-replenishing process to the Fe center, a facile CO_2 binding process would not occur because it would suffer from a large reorganization energy arising from changes in the first coordination sphere of the Fe center. A detailed mechanistic study following this reasoning is in progress in our laboratory.

4. CONCLUSION

The present work describes a detailed study of the electronic structure of the triplet ground state of complex **1** using a combined spectroscopic and computational approach. Neither theory nor experiment alone can unequivocally assign its ground state because of the near-degeneracy of the $^3A_{2g}$ and ^3E_g electronic states. To this end, an EH was proposed, which explicitly takes the SOC and Zeeman interactions of $^3A_{2g}$ and ^3E_g into account. This model enabled us to successfully simulate all VTVH magnetometry, ^{57}Fe Mössbauer, and THz-EPR data by optimizing only three adjustable parameters. Our results show that the $^3A_{2g}$ electronic state lies energetically below ^3E_g [with dominant $^3E_g(A)$ parentage] but only by 950 cm^{-1}. Therefore, the low-lying triplet is a SOC-induced admixture of $^3A_{2g}$ (<88%) and ^3E_g (>12%), and the lowest-energy singlet possesses substantial unquenched orbital angular momentum in the *xy* plane. In comparison with uniaxial systems featuring orbitally nearly doubly degenerate ground states with unquenched orbital angular momenta in one direction, the electronic ground state of complex **1** is best interpreted as having an electronic ground state with accidental almost triple degeneracy, a truly multiconfigurational state indeed. Experimentally, this unusual electronic structure is manifested by its peculiar magnetic properties, viz., a large axial ZFS of +94 cm^{-1}, two large *g* components along the *xy* directions of ∼3, an effective magnetic moment of 4.2 μ_B, and, most importantly, a large and positive internal field at the ^{57}Fe nucleus in the *xy* plane.

Through a comparison with related systems, we found the following spectroscopic signature to differentiate systems whose electronic ground states have 2- or 3-fold near-degeneracy with more than half-filled quasi-degenerate orbitals. For nearly triply degenerate systems, their low-lying spin manifolds likely feature easy-plane anisotropy ($g_\parallel \ll g_\perp$), whereas for almost doubly degenerate complexes, their low-lying spin manifolds are probably distinguished by easy-axis anisotropy ($g_\parallel \gg g_\perp$). Finally, implications of the electronic structure of **1** to CO_2 reduction are discussed.

■ ASSOCIATED CONTENT

Supporting Information

The Supporting Information is available free of charge at https://pubs.acs.org/doi/10.1021/acs.inorgchem.1c00031.

> Δ_{A-E} energy gap description in the literature, graphical depiction of the orbitals in the active space for **1**, supplementary magnetometry, ^{57}Fe Mössbauer, and THz-EPR data, state composition of the symmetry-adapted magnetic sublevels, detailed investigation of the effect of inclusion of the $^5A_{1g}$ state in the EH, details about the calculation of SH parameters, and the relative failure of the SH (PDF)

■ AUTHOR INFORMATION

Corresponding Authors

Frank Neese − *Max-Planck-Institut für Kohlenforschung, D-45470 Mülheim an der Ruhr, Germany*; orcid.org/0000-0003-4691-0547; Email: neese@kofo.mpg.de

Eckhard Bill − *Max-Planck-Institut für Chemische Energiekonversion, D-45470 Mülheim an der Ruhr, Germany*; orcid.org/0000-0001-9138-3964; Email: eckhard.bill@cec.mpg.de

Shengfa Ye − *State Key Laboratory of Catalysis, Dalian Institute of Chemical Physics, Chinese Academy of Sciences, Dalian 116023, China; Max-Planck-Institut für Kohlenforschung, D-45470 Mülheim an der Ruhr, Germany*; orcid.org/0000-0001-9747-1412; Email: shengfa.ye@dicp.ac.cn

Authors

Maxime Tarrago − *Max-Planck-Institut für Kohlenforschung, D-45470 Mülheim an der Ruhr, Germany*

Christina Römelt − *Max-Planck-Institut für Chemische Energiekonversion, D-45470 Mülheim an der Ruhr, Germany*; orcid.org/0000-0003-1673-1484

Joscha Nehrkorn − *Max-Planck-Institut für Chemische Energiekonversion, D-45470 Mülheim an der Ruhr, Germany*

Alexander Schnegg − *Max-Planck-Institut für Chemische Energiekonversion, D-45470 Mülheim an der Ruhr, Germany*; orcid.org/0000-0002-2362-0638

Complete contact information is available at: https://pubs.acs.org/10.1021/acs.inorgchem.1c00031

Notes

The authors declare no competing financial interest.

■ ACKNOWLEDGMENTS

We gratefully acknowledge generous financial support from the European Union Marie Sklodowska Curie Initial Training NoNoMeCat (Grant 675020-MSCA-ITN-2015-ETN) and the Max-Planck Society, in particular, the joint workspace of MPI

Chemische Energiekonversion and MPI Kohlenforschung. We also thank HZB for the allocation of synchrotron radiation beamtime and Karsten Holldack and Dirk Ponwitz for their support during the THz-EPR experiments.

■ DEDICATION

This work is dedicated to Prof. Dr. Wolfgang Kaim on the occasion of his 70th birthday.

■ REFERENCES

(1) (a) Baglia, R. A.; Zaragoza, J. P. T.; Goldberg, D. P. Biomimetic reactivity of oxygen-derived manganese and iron porphyrinoid complexes. *Chem. Rev.* **2017**, *117*, 13320−13352. (b) Zhang, W.; Lai, W.; Cao, R. Energy-related small molecule activation reactions: oxygen reduction and hydrogen and oxygen evolution reactions catalyzed by porphyrin- and corrole-based systems. *Chem. Rev.* **2017**, *117*, 3717−3797.

(2) (a) Schlögl, R. Put the sun in the tank: future developments in sustainable energy systems. *Angew. Chem., Int. Ed.* **2019**, *58*, 343−348. (b) Al-Mamoori, A.; Krishnamurthy, A.; Rownaghi, A. A.; Rezaei, F. Carbon capture and utilization update. *Energy Technol.* **2017**, *5*, 834−849.

(3) (a) Azcarate, I.; Costentin, C.; Robert, M.; Savéant, J. M. Through-space charge interaction substituent effects in molecular catalysis leading to the design of the most efficient catalyst of CO_2-to-CO electrochemical conversion. *J. Am. Chem. Soc.* **2016**, *138*, 16639−16644. (b) Costentin, C.; Passard, G.; Robert, M.; Savéant, J. M. Pendant acid-base groups in molecular catalysis: H-bond promoters or proton relays? Mechanism of the conversion of CO_2 to CO by electrogenerated iron(0)Porphyrins bearing prepositioned phenol functionalities. *J. Am. Chem. Soc.* **2014**, *136*, 11821−11829. (c) Costentin, C.; Passard, G.; Robert, M.; Savéant, J. M. Ultraefficient homogeneous catalyst for the CO_2-to-CO electrochemical conversion. *Proc. Natl. Acad. Sci. U. S. A.* **2014**, *111*, 14990−14994. (d) Costentin, C.; Drouet, S.; Passard, G.; Robert, M.; Savéant, J. M. Proton-coupled electron transfer cleavage of heavy-atom bonds in electrocatalytic processes. Cleavage of a C-O bond in the catalyzed electrochemical reduction of CO_2. *J. Am. Chem. Soc.* **2013**, *135*, 9023−9031. (e) Costentin, C.; Drouet, S.; Robert, M.; Savéant, J. M. A local proton source enhances CO_2 electroreduction to CO by a molecular Fe catalyst. *Science* **2012**, *338*, 90−94.

(4) Azcarate, I.; Costentin, C.; Robert, M.; Savéant, J. M. Through-space charge interaction substituent effects in molecular catalysis leading to the design of the most efficient catalyst of CO_2-to-CO electrochemical conversion. *J. Am. Chem. Soc.* **2016**, *138*, 16639−16644.

(5) (a) Römelt, C.; Song, J.; Tarrago, M.; Rees, J. A.; van Gastel, M.; Weyhermüller, T.; Debeer, S.; Bill, E.; Neese, F.; Ye, S. Electronic structure of a formal iron(0) porphyrin complex relevant to CO_2 reduction. *Inorg. Chem.* **2017**, *56*, 4745−4750. (b) Römelt, C.; Ye, S.; Bill, E.; Weyhermüller, T.; van Gastel, M.; Neese, F. Electronic structure and spin multiplicity of iron tetraphenylporphyrins in their reduced states as determined by a combination of resonance Raman spectroscopy and quantum chemistry. *Inorg. Chem.* **2018**, *57*, 2141−2148.

(6) Kobayashi, H.; Yanagawa, Y. Electronic spectra and electronic structure of iron(II) tetraphenylporphyrins. *Bull. Chem. Soc. Jpn.* **1972**, *45*, 450−456.

(7) (a) Collman, J. P.; Hoard, J. L.; Kim, N.; Lang, G.; Reed, C. A. Synthesis, stereochemistry and structure-related properties of *α,β,γ,δ*-Tetraphenylporphyrinatoiron(II). *J. Am. Chem. Soc.* **1975**, *97*, 2676−2681. (b) Hu, C.; Noll, B. C.; Schulz, C. E.; Scheidt, W. R. Four-coordinate iron(II) porphyrinates: electronic configuration change by intermolecular interaction. *Inorg. Chem.* **2007**, *46*, 619−621. (c) Boyd, P. D. W.; Buckingham, D. A.; McMeeking, R. F.; Mitra, S. Paramagnetic anisotropy, average magnetic susceptibility, and electronic structure of intermediate-spin S = 1 (5,10,15,10-tetraphenylporphyrin)iron(II). *Inorg. Chem.* **1979**, *18*, 3585−3591.

(8) (a) Behere, D. V.; Birdy, R.; Mitra, S. Effect of axial interaction in high-spin iron(III) porphyrins. Paramagnetic anisotropy and zero-field splitting in (tetraphenylporphyrin)iron(III) thiocyanate and and iodide. *Inorg. Chem.* **1981**, *20*, 2786−2789. (b) Hatano, K.; Scheidt, W. R. Molecular stereochemistry of iodo(mesa-tetraphenylporphinato)iron(III). *Inorg. Chem.* **1979**, *18*, 877−879.

(9) Scheidt, W. R.; Kastner, M. E.; Hatano, K. Stereochemistry of the toluene solvate of *α,β,γ,δ*-tetraphenylporphyrinatozinc(II). *Inorg. Chem.* **1978**, *17*, 706−710.

(10) Sontum, S. F.; Case, D. A.; Karplus, M. Xa multiple scattering calculations on iron(II) porphine. *J. Chem. Phys.* **1983**, *79*, 2881−2892.

(11) Obara, S.; Kashiwagi, H. Ab-initio MO studies of electronic states and Mössbauer spectra of high-, intermediate-, and low-spin Fe(II)-porphyrin complexes. *J. Chem. Phys.* **1982**, *77*, 3155−3165.

(12) Kitagawa, T.; Teraoka, J. The resonance Raman spectra of intermediate-spin ferrous porphyrin. *Chem. Phys. Lett.* **1979**, *63*, 443−446.

(13) Tanaka, K.; Elkaim, E.; Li, L.; Jue, Z. N.; Coppens, P.; Landrum, J. Electron density studies of porphyrins and phthalocyanines. IV. Electron density distribution in crystals of (meso-tetraphenylporphinato) iron (II). *J. Chem. Phys.* **1986**, *84* (12), 6969−6978.

(14) Goff, H.; LaMar, G. N.; Reed, C. A. Nuclear magnetic resonance investigation of magnetic and electronic properties of "intermediate spin" ferrous porphyrin complexes. *J. Am. Chem. Soc.* **1977**, *99*, 3641−3646.

(15) Lang, G.; Spartalian, K.; Reed, C. A.; Collman, J. P. Mössbauer effect study of the magnetic properties of S = 1 ferrous tetraphenylporphyrin. *J. Chem. Phys.* **1978**, *69*, 5424−5427.

(16) (a) Choe, Y.-K.; Hashimoto, T.; Nakano, H.; Hirao, K. Theoretical study of the electronic ground state of iron(II) porphine. *Chem. Phys. Lett.* **1998**, *295*, 380−388. (b) Choe, Y. K.; Nakajima, T.; Hirao, K.; Lindh, R. Theoretical study of the ground state of the electronic ground state of iron(II) porphine. II. *J. Chem. Phys.* **1999**, *111*, 3837.

(17) Radón, M. Spin-state energetics of heme-related models from DFT and coupled-cluster calculations. *J. Chem. Theory Comput.* **2014**, *10*, 2306−2321.

(18) Li Manni, G.; Alavi, A. Understanding the mechanism stabilizing intermediate spin states in Fe(II)-porphyrin. *J. Phys. Chem. A* **2018**, *122*, 4935−4947.

(19) Rawlings, D. C.; Gouterman, M.; Davidson, E. R.; Feller, D. Theoretical investigations of the electronic states of porphyrins. III. Low-lying electronic states of porphinatoiron(II). *Int. J. Quantum Chem.* **1985**, *28*, 773−796.

(20) (a) Hirao, K. Multireference Møller-Plesset method. *Chem. Phys. Lett.* **1992**, *190*, 374−380. (b) Hirao, K. Multireference Møller-Plesset perturbation theory for high-spin open-shell systems. *Chem. Phys. Lett.* **1992**, *196*, 397−403. (c) Hirao, K. State-specific multireference Møller-Plesset perturbation treatment for singlet and triplet excited states, ionized states and electron attached states of H_2O. *Chem. Phys. Lett.* **1993**, *201*, 59−66. (d) Hirao, K. Multireference Møller-Plesset perturbation treatment of potential energy curve of N_2. *Int. J. Quantum Chem.* **1992**, *44*, 517−526.

(21) Pierloot, K.; Phung, Q. M.; Domingo, A. Spin state energetics in first-row transition metal complexes: contribution of (3s3p) correlation and its description by second-order perturbation theory. *J. Chem. Theory Comput.* **2017**, *13*, 537−553.

(22) Altun, A.; Saitow, M.; Neese, F.; Bistoni, G. Local energy decomposition of open-shell molecular systems in the Domain-Based Local Pair Natural Orbital Coupled Cluster framework. *J. Chem. Theory Comput.* **2019**, *15*, 1616−1632.

(23) Merrill, B. A. *Encyclopedia of Reagents for Organic Synthesis*; John Wiley and Sons, Ltd., 2001.

(24) Mashiko, T.; Reed, C. A.; Haller, K. J.; Scheidt, W. R. Nature of iron(I) and iron(0) tetraphenylporphyrin complexes. Synthesis and molecular structure of (dibenzo-18-crown-6)bis(tetrahydrofuran) sodium (meso-tetraphenylporphinato)ferrate and bis[tris-

(tetrahydrofuran)sodium](meso-tetraporphinato)ferrate. *Inorg. Chem.* **1984**, *23*, 3192−3196.

(25) (a) Nehrkorn, J.; Holldack, K.; Bittl, R.; Schnegg, A. Recent progress in synchrotron-based frequency-domain fourier-transform THz-EPR. *J. Magn. Reson.* **2017**, *280*, 10−19. (b) Nehrkorn, J.; Martins, B. M.; Holldack, K.; Stoll, S.; Dobbek, H.; Bittl, R.; Schnegg, A. zero-field splittings in MetHb and MetMb with aquo and fluoro ligands: a FD-FT THz-EPR study. *Mol. Phys.* **2013**, *111*, 2696−2707. (c) Schnegg, A.; Behrends, J.; Lips, K.; Bittl, R.; Holldack, K. Frequency Domain Fourier Transform THz-EPR on single molecule magnets using coherent synchrotron radiation. *Phys. Chem. Chem. Phys.* **2009**, *11*, 6820−6825.

(26) Stoll, S.; Schweiger, A. EasySpin, a comprehensive software package for spectral simulation and analysis in EPR. *J. Magn. Reson.* **2006**, *178*, 42−55.

(27) (a) Nehrkorn, J.; Schnegg, A.; Holldack, K.; Stoll, S. General magnetic transition dipole moments for electron paramagnetic resonance. *Phys. Rev. Lett.* **2015**, *114*, 010801. (b) Nehrkorn, J.; Telser, J.; Holldack, K.; Stoll, S.; Schnegg, A. Simulating frequency-domain electron paramagnetic resonance: bridging the gap between experiment and magnetic parameters for high-spin transition-metal ion complexes. *J. Phys. Chem. B* **2015**, *119*, 13816−13824.

(28) Ikezaki, A.; Nakamura, M. Effects of solvents on the electron configurations of the low-spin dicyano[meso-tetrakis(2,4,6-triethylphenyl)porphyrinato]iron(III) complex: importance of the C-H···N weak hydrogen bonding. *Inorg. Chem.* **2002**, *41*, 2761−2768.

(29) Becke, A. D. Density-functional exchange-energy approximation with correct asymptotic behavior. *Phys. Rev. A: At., Mol., Opt. Phys.* **1988**, *38*, 3098.

(30) Weigend, F.; Ahlrichs, R. Balanced basis sets of split valence, triple zeta valence and quadrupole zeta valence quality for H to Rn: Design and assessment of accuracy. *Phys. Chem. Chem. Phys.* **2005**, *7*, 3297−3305.

(31) Grimme, S.; Ehrlich, S.; Goerigk, L. Effect of the damping function in dispersion corrected Density Functional Theory. *J. Comput. Chem.* **2011**, *32* (7), 1456−1465.

(32) Neese, F. An improvement of the resolution of the identity approximation for the formation of the Coulomb matrix. *J. Comput. Chem.* **2003**, *24* (14), 1740−1747.

(33) Malmqvist, P.-Å.; Roos, B. O. The CASSCF State interaction method. *Chem. Phys. Lett.* **1989**, *155* (2), 189−194.

(34) Neese, F. Importance of direct spin− spin coupling and spin-flip excitations for the zero-field splittings of transition metal complexes: a case study. *J. Am. Chem. Soc.* **2006**, *128* (31), 10213−10222.

(35) Radon, M.; Pierloot, K. Binding of CO, NO and O_2 to heme by density functional and multireference ab-initio calculations. *J. Phys. Chem. A* **2008**, *112*, 11824−11832.

(36) (a) Angeli, C.; Cimiraglia, R.; Evangelisti, S.; Leininger, T.; Malrieu, J. P. Introduction of n-electron valence states for multi-reference perturbation theory. *J. Chem. Phys.* **2001**, *114*, 10252−10264. (b) Angeli, C.; Cimiraglia, R.; Malrieu, J. P. N-electron valence state perturbation theory: A spinless formulation and an efficient implementation of the strongly contracted and of the partially contracted variant. *J. Chem. Phys.* **2002**, *117*, 9138−9153.

(37) Neese, F. Software update: the ORCA program system, version 4.0. *WIREs Comput. Mol. Sci.* **2018**, *8*, e1327.

(38) Kahn, O. *Molecular Magnetism*; VCH Publishers, 1993; pp 7 and 8.

(39) Strauss, S. H.; Pawlik, M. J. Ring-induced rhombicity in chlorin and isobacteriochlorin complexes of square-planar iron (II). *Inorg. Chem.* **1986**, *25*, 1921−1923.

(40) Reed, C. A.; Mashiko, T.; Scheidt, W. R.; Spartalian, K.; Lang, G. High-spin iron (II) in the porphyrin plane. Structural characterization of (meso-tetraphenylporphinato) bis (tetrahydrofuran) iron (II). *J. Am. Chem. Soc.* **1980**, *102*, 2302−2306.

(41) Atanasov, M.; Aravena, D.; Suturina, E.; Bill, E.; Maganas, D.; Neese, F. First principles approach to the electronic structure, magnetic anisotropy and spin relaxation in mononuclear 3d-transition metal single molecule magnets. *Coord. Chem. Rev.* **2015**, *289-290*, 177−214.

(42) McGarvey, B. R.; Telser, J. Simple ligand-field theory of d^4 and d^6 transition metal complexes with a C_3 symmetry axis. *Inorg. Chem.* **2012**, *51*, 6000−6010.

(43) Carlin, R. L. *Magnetochemistry*; Springer-Varlag: Berlin, 1986; p 12.

(44) Strauss, S. H.; Silver, M. E.; Long, K. M.; Thompson, R. G.; Hudgens, R. A.; Spartalian, K.; Ibers, J. A. Comparison of the molecular and electronic structure of (2,3,7,8,12,13,17,18-octaethylporphyrinato)iron(II) and (trans-7,8-Dihydro-2,3,7,8,12,13,17,18-octaethylporphyrinato)iron(II). *J. Am. Chem. Soc.* **1985**, *107*, 4207−4215.

(45) Dolphin, D.; Sams, J. R.; Tsin, T. B.; Wong, K. L. Synthesis and Mössbauer spectra of octaethylporphyrin ferrous complexes. *J. Am. Chem. Soc.* **1976**, *98*, 6970−6975.

(46) Gütlich, P.; Bill, E.; Trautwein, A. X. *Mössbauer spectroscopy and transition metal chemistry*; Springer-Verlag: Berlin, 2011.

(47) (a) Schapiro, I.; Sivalingam, K.; Neese, F. Assessment of n-electron valence state perturbation theory for vertical excitation energies. *J. Chem. Theory Comput.* **2013**, *9*, 3567−3580. (b) Bhattacharjee, A.; Chavarot-Kerlidou, M.; Dempsey, J. L.; Gray, H. B.; Fujita, E.; Muckerman, J. T.; Fontecave, M.; Artero, V.; Arantes, G. M.; Field, M. J. Theoretical modeling of low-energy electronic absorption bands in reduced cobaloximes. *ChemPhysChem* **2014**, *15*, 2951−2958.

(48) Dunn, T. M. Spin-orbit coupling in the first and second transition series. *Trans. Faraday Soc.* **1961**, *57*, 1441−1444.

(49) Neese, F. *Magnetism: Molecules to Material IV*, Miller, J. S., Drillon, M., Eds.; Wiley, 2002; p 386.

(50) (a) Maltempo, M. M. Magnetic state of an unusual bacterial heme protein. *J. Chem. Phys.* **1974**, *61* (7), 2540−2547. (b) Maltempo, M.; Moss, T.; Spartalian, K. Mossbauer spectroscopy of the mixed-spin and high-spin states of Chromatium Ferricytochrome C′. *J. Chem. Phys.* **1980**, *73* (5), 2100−2106. (c) Okamoto, T.; Ohmichi, E.; Okubo, S.; Ohta, H. Precise determination of zero-field splitting parameters of hemin by high-field and high-frequency Electron Paramagnetic Resonance. *J. Phys. Soc. Jpn.* **2018**, *87* (1), 013702. (d) Viciano-Chumillas, M.; Blondin, G.; Clémancey, M.; Krzystek, J.; Ozerov, M.; Armentano, D.; Schnegg, A.; Lohmiller, T.; Telser, J.; Lloret, F.; Cano, J. Single-ion magnetic behaviour in an iron (III) porphyrin complex: a dichotomy between high spin and 5/2−3/2 spin admixture. *Chem. - Eur. J.* **2020**, *26* (62), 14242−14251.

(51) Abragam, A. *The Principles of Nuclear Magnetism*; Oxford University Press, 1961; pp 171 and 172.

(52) Griffith, J. S. *The Theory of Transition Metal Ions*; Cambridge University Press, 1961; p 325.

(53) (a) Reiff, W. M.; Frommen, C. M.; Yee, G. T.; Sellers, S. P. Observation of a very large internal hyperfine field (62.4T) in the ferromagnetically-ordered state of the $S = 1$ α-iron(II) octaethyltetraazaporphyrin. *Inorg. Chem.* **2000**, *39*, 2076−2079. (b) Greenwood, N. N.; Gibb, T. C. *Mössbauer Spectroscopy*; Chapman and Hall, 1971. (c) Johnson, C. E. Hyperfine interactions in ferrous fluorsilicate. *Proc. Phys. Soc., London* **1967**, *92*, 748−757. (d) Oosterhuis, W. T.; Lang, G. Mössbauer effect in $K_3Fe(CN)_6$. *Phys. Rev.* **1969**, *178*, 439−456. (e) Lang, G.; Marshall, W. Mössbauer effect in some haemoglobin compounds. *J. Mol. Biol.* **1966**, *18*, 385−404. (f) Johnson, C. E. Mössbauer effect in some haemoglobin compounds. *Phys. Lett.* **1966**, *21*, 491−492. (g) Lang, G. Mössbauer spectroscopy of haem proteins. *Q. Rev. Biophys.* **1970**, *3*, 1−60.

(54) Ganyushin, D.; Neese, F. First-principles calculations of zero-field splitting parameters. *J. Chem. Phys.* **2006**, *125*, 024103.

(55) Chibotaru, L. F.; Ungur, L. Ab-initio calculation of anisotropic magnetic properties of complexes. I. Unique definition of pseudospin Hamiltonians and their derivation. *J. Chem. Phys.* **2012**, *137*, 064112.

(56) Abragam, A.; Pryce, M. H. L. The theory of paramagnetic resonance in hydrated cobalt salts. *Proc. R. Soc. London A* **1951**, *206*, 173−191.

(57) (a) Myers, W. K.; Scholes, C. P.; Tierney, D. L. Anisotropic Fermi couplings due to large unquenched orbital angular momentum: Q-band (1)H, (14)N, and (11)B ENDOR of bis(trispyrazolylborate) cobalt(II). *J. Am. Chem. Soc.* **2009**, *131*, 10421−10429. (b) McGarvey, B. R.; Nagy, S. Evidence for an anisotropic contact shift. Proton NMR study of line shapes in uranocene and tricyclopentadienyl uranium chloride, $(C_5H_5)_3UCl$, powders. *Inorg. Chem.* **1987**, *26*, 4198−4203.

(58) (a) Walker, F. A. Magnetic spectroscopic (EPR, ESEEM, Mössbauer, MCD and NMR) studies of low-spin ferriheme centers and their corresponding heme proteins. *Coord. Chem. Rev.* **1999**, *185*, 471−534. (b) Taylor, C. P. S. The EPR of low-spin heme complexes relation of the t_{2g} hole model to the directional properties of the g-tensor, and a new method for calculating the ligand-field parameters. *Biochim. Biophys. Acta, Protein Struct.* **1977**, *491*, 137−149. (c) McGarvey, B. R. Survey of ligand field parameters of strong field d^5 complexes obtained from the g matrix. *Coord. Chem. Rev.* **1998**, *170*, 75−92. (d) McGarvey, B. R. The ESR g matrix for strong field d^5 systems. *Quim. Nova* **1998**, *21*, 206−213.

(59) Safo, M. K.; Walker, F. A.; Raitsimring, A. M.; Walters, W. P.; Dolata, D. P.; Debrunner, P. G.; Scheidt, W. R. Axial ligand orientation in iron(III) porphyrinates: effect of axial.pi.-acceptors. Characterization of the low-spin complex $[Fe(TPP)(4\text{-}CNPy)_2]ClO_4$. *J. Am. Chem. Soc.* **1994**, *116*, 7760−7770.

(60) Walker, F. A.; Nasri, H.; Turowska-Tyrk, I.; Mohanrao, K.; Watson, C. T.; Shokhirev, N. V.; Debrunner, P. G.; Scheidt, W. R. π-Acid ligands in iron(III) porphyrinates. characterization of low-spin bis(tert-butylisocyanide)(porphyrinato)iron(III) complexes having $(d_{xz},d_{yz})^4(d_{xy})^1$ ground states. *J. Am. Chem. Soc.* **1996**, *118*, 12109−12118.

(61) (a) Assour, J. Electron spin resonance of tetraphenylporphine chelates. *J. Chem. Phys.* **1965**, *43*, 2477−2489. (b) Iwaizumi, M.; Ohba, Y.; Iida, H.; Hirayama, M. EPR and ENDOR studies of charge transfer interaction of cobalt(II) and copper(II) porphyrins with π-donors and acceptors. *Inorg. Chim. Acta* **1984**, *82*, 47−52. (c) Baumgarten, M.; Winscom, C. J.; Lubitz, W. Probing the surrounding o a cobalt(II) porphyrin and its superoxo complex by EPR technique. *Appl. Magn. Reson.* **2001**, *20*, 35−70. (d) Walker, F. A. ESR studies of Co(II) tetraphenylporphyrins and their oxygen adducts: Complex formation with aromatic molecules and sterically hindered lewis bases. *J. Magn. Reson.* **1974**, *15*, 201−218.

(62) (a) Lin, W. C. d-Orbital energies and low-lying excited states of cobalt porphyrins. *Inorg. Chem.* **1976**, *15*, 1114−1118. (b) Lin, W. C. Further work on the calculation of d-orbital energies of cobalt porphyrins from electron spin resonance data. *Inorg. Chem.* **1980**, *19*, 1072−1073.

(63) Filoti, G.; Kuz'min, M. D.; Bartolomé, J. Mössbauer study of the hyperfine interactions and spin dynamics in α-iron(II) phthalocyanine. *Phys. Rev. B: Condens. Matter Mater. Phys.* **2006**, *74*, 134420.

(64) (a) Sellers, S. P.; Korte, B. J.; Fitzgerald, J. P.; Reiff, W. M.; Yee, G. T. Canted ferromagnetism and other magnetic phenomena in square-planar, neutral manganese (II) and iron (II) octaethyltetraazaporphyrins. *J. Am. Chem. Soc.* **1998**, *120*, 4662−4670. (b) Dale, B. W.; Williams, R. J. P.; Johnson, C. E.; Thorp, T. S = 1 Spin state of divalent iron. I. Magnetic properties of phthalocyanine iron (II). *J. Chem. Phys.* **1968**, *49*, 3441−3444. (c) Dale, B. W.; Williams, R. J. P.; Edwards, P.; Johnson, C. E. S = 1 spin state of divalent Iron. II. A Mössbauer-effect study of phthalocyanine iron (II). *J. Chem. Phys.* **1968**, *49*, 3445−3449. (d) Barraclough, C.; Martin, R.; Mitra, S.; Sherwood, R. Paramagnetic anisotropy, low temperature magnetization, and electronic structure of Iron (II) phthalocyanine. *J. Chem. Phys.* **1970**, *53*, 1643−1648. (e) Dale, B. Evidence from Mössbauer spectroscopy of a departure from tetragonal symmetry in the phthalocyanineiron (II) molecule. *Mol. Phys.* **1974**, *28*, 503−511.

(65) (a) Zadrozny, J. M.; Atanasov, M.; Bryan, A.; Lin, C.-Y.; Rekken, B. D.; Power, P. P.; Neese, F.; Long, J. R. Slow magnetization dynamics in a series of two-coordinate iron(II) complexes. *Chem. Sci.* **2013**, *4*, 125−138. (b) Merrill, W. A.; Stich, T. A.; Brynda, M.; Yeagle, G. J.; Fettinger, J. C.; De Hont, R.; Reiff, W. M.; Schulz, C. E.; Britt, R. D.; Power, P. P. Direct spectroscopic observation of large quenching of first-order orbital angular momentum with bending in monomeric, two-coordinate Fe(II) primary amido complexes and the profound magnetic effects in the absence of Jahn-Teller and Renner-Teller distortions in rigorously linear coordination. *J. Am. Chem. Soc.* **2009**, *131*, 12693−12702. (c) Cheng, J.; Liu, J.; Leng, X.; Lohmiller, T.; Schnegg, A.; Bill, E.; Ye, S.; Deng, L. A two-coordinate iron(II) imido complex with NHC ligation: synthesis, characterization, and its diversified reactivity of nitrene transfer and C−H bond activation. *Inorg. Chem.* **2019**, *58*, 7634−7644. (d) Zadrozny, J. M.; Xiao, D. J.; Long, J. R.; Atanasov, M.; Neese, F.; Grandjean, F.; Long, G. J. Mössbauer spectroscopy as a probe of magnetization dynamics in the linear iron(I) and iron(II) complexes $[Fe(C(SiMe_3)_3)_2]^{1-/0}$. *Inorg. Chem.* **2013**, *52*, 13123−13131. (e) Bryan, A. M.; Lin, C.-Y.; Sorai, M.; Miyazaki, Y.; Hoyt, H. M.; Hablutzel, A.; LaPointe, A.; Reiff, W. M.; Power, P. P.; Schulz, C. E. Measurement of extreme hyperfine fields in two-coordinate high spin Fe^{2+} complexes by Mössbauer spectroscopy: essentially free ion magnetism in the solid state. *Inorg. Chem.* **2014**, *53*, 12100−12107. (f) Reiff, W. M.; Schulz, C. E.; Whangbo, M.-H.; Seo, J. I.; Lee, Y. S.; Potratz, G. R.; Spicer, C. W.; Girolami, G. S. Consequences of a linear two-coordinate geometry for the orbital magnetism and Jahn-Teller distortion behavior of the high spin iron(II) complex $Fe[N(t\text{-}Bu)_2]_2$. *J. Am. Chem. Soc.* **2009**, *131*, 404−405. (g) Reiff, W. M.; LaPointe, A. M.; Witten, E. H. Virtual free ion magnetism and the absence of Jahn-Teller distortion in a linear two-coordinate complex of high-spin iron(II). *J. Am. Chem. Soc.* **2004**, *126*, 10206−10207.

(66) Andres, H.; Bominaar, E. L.; Smith, J. M.; Eckert, N. A.; Holland, P. L.; Münck, E. Planar three-coordinate high-spin Fe^{II} complexes with large orbital angular momentum: Mössbauer, Electron Paramagnetic Resonance, and electronic structure studies. *J. Am. Chem. Soc.* **2002**, *124*, 3012−3025.

(67) Zoppellaro, G.; Bren, K. L.; Ensign, A. A.; Harbitz, E.; Kaur, R.; Hersleth, H.-P.; Ryde, U.; Hederstedt, L.; Andersson, K. K. Studies of ferric heme proteins with highly anisotropic/highly axial low spin (S = 1/2) electron paramagnetic resonance signals with bis-histidine and histidine-methionine axial iron coordination. *Biopolymers* **2009**, *91*, 1064−1082.

(68) Stoian, S. A.; Yu, Y.; Smith, J. M.; Holland, P. L.; Bominaar, E. L.; Münck, E. Mössbauer, Electron Paramagnetic Resonance and crystallographic characterization of a high-spin Fe(I) diketiminate complex with orbital degeneracy. *Inorg. Chem.* **2005**, *44*, 4915−4922.

(69) (a) Neese, F.; Solomon, E. I. Calculation of zero-field splittings, g-values, and the relativistic nephelauxetic effect in transition metal complexes. Application to high-spin ferric complexes. *Inorg. Chem.* **1998**, *37*, 6568−6582. (b) Mabbs, F. E.; Collison, D. *Electron Paramagnetic Resonance of d Transition Metal Compounds*; Elsevier Science: Amsterdam, The Netherlands, 1992; p 17. (c) Atherton, N. M. *Principles of Electron Spin Resonance*; Ellis Horwood Ltd.: Chichester, England, 1993. (d) Weil, J. A.; Bolton, J. R. *Electron Paramagnetic Resonance—Elementary Theory and Practical Applications*; John Wiley & Sons, Inc.: Hoboken, NJ, 2007. (e) Carrington, A.; McLachlan, A. D. *Introduction to Magnetic Resonance*; Harper & Row and John Weatherhill: New York and Tokyo, 1969.

(70) Chang, H.-C.; Mondal, B.; Fang, H.; Neese, F.; Bill, E.; Ye, S. Electron Paramagnetic Resonance signature of tetragonal low spin iron(V)-nitrido and -oxo complexes derived from the electronic structure analysis of heme and non-heme archetypes. *J. Am. Chem. Soc.* **2019**, *141*, 2421−2434.

(71) Bijl, D. Paramagnetic resonance absorption in titanium caesium alum at low temperatures. *Proc. Phys. Soc., London, Sect. A* **1950**, *63*, 405−406.

(72) (a) Tregenna-Piggott, P. L. W.; Güdel, H.-U. Influence of Jahn−Teller coupling on the magnetic properties of transition metal complexes with orbital triplet ground terms: magnetization and electronic Raman studies of the titanium(III) hexa-aqua cation. *Inorg. Chem.* **2001**, *40*, 5497−5506. (b) Tregenna-Piggott, P. L. W.; Best, S. P. Single-crystal Raman spectroscopy of the rubidium alums $RbM^{III}(SO_4)_2\cdot 12H_2O$ (M^{III} = Al, Ga, In, Ti, V, Cr, Fe) between

275 and 1200 cm-1: correlation between the electronic structure of the tervalent cation and structural abnormalities. *Inorg. Chem.* **1996**, *35*, 5730−5736.

(73) (a) MacKinnon, J. A.; Dionne, G. F. Electron paramagnetic resonance of Ti^{3+} ions in $TiAl(SO_4)_2$•$12H_2O$. *Can. J. Phys.* **1966**, *44*, 2329−2335. (b) Dionne, G. F.; MacKinnon, J. A. Origin of the crystal field in Ti^{3+}-substituted alums. *Phys. Rev.* **1968**, *172*, 325−330. (c) Maurelli, S.; Livraghi, S.; Chiesa, M.; Giamello, E.; Van Doorslaer, S.; Di Valentin, C.; Pacchioni, G. Hydration structure of the Ti(III) cation as revealed by pulse EPR and DFT studies: new insights into a textbook Case. *Inorg. Chem.* **2011**, *50*, 2385−2394.

(74) (a) Bleaney, B. Anisotropy in titanium alum. *Proc. Phys. Soc., London, Sect. A* **1950**, *63*, 407−408. (b) Carlin, R. L. *Magnetochemistry*; Springer-Varlag, Berlin, 1986; p 28.

(75) Caulfield, K. P.; Conradie, J.; Arman, H. D.; Ghosh, A.; Tonzetich, Z. J. Iron(II) corrole anions. *Inorg. Chem.* **2019**, *58*, 15225−15235.

(76) (a) Froehlich, J. D.; Kubiak, C. P. Homogeneous CO_2 reduction by Ni(cyclam) at a glassy carbon electrode. *Inorg. Chem.* **2012**, *51*, 3932−3934. (b) Froehlich, J. D.; Kubiak, C. P. The homogeneous reduction of CO_2 by $[Ni(cyclam)]^+$: increased catalytic rates with the addition of a CO Scavenger. *J. Am. Chem. Soc.* **2015**, *137*, 3565−3573. (c) Jiang, C.; Nichols, A. W.; Walzer, J. F.; Machan, C. W. Electrochemical CO_2 reduction in a continuous non-aqueous flow cell with $[Ni(cyclam)]^{2+}$. *Inorg. Chem.* **2020**, *59*, 1883−1892.

(77) Song, J.; Klein, E. L.; Neese, F.; Ye, S. The mechanism of homogeneous CO_2 reduction by Ni(cyclam): product selectivity, concerted proton−electron transfer and C−O bond cleavage. *Inorg. Chem.* **2014**, *53*, 7500−7507.